© 2016. Published by The Company of Biologists Ltd | Development (2016) 143, 810-821 doi:10.1242/dev.132688

RESEARCH ARTICLE

KMT2D regulates specific programs in heart development via histone H3 lysine 4 di-methylation

Siang-Yun Ang[1,2,3], Alec Uebersohn[1,2], C. Ian Spencer[1,2,*], Yu Huang[1,2], Ji-Eun Lee[4], Kai Ge[4] and Benoit G. Bruneau[1,2,3,5,6,‡]

ABSTRACT

KMT2D, which encodes a histone H3K4 methyltransferase, has been implicated in human congenital heart disease in the context of Kabuki syndrome. However, its role in heart development is not understood. Here, we demonstrate a requirement for KMT2D in cardiac precursors and cardiomyocytes during cardiogenesis in mice. Gene expression analysis revealed downregulation of ion transport and cell cycle genes, leading to altered calcium handling and cell cycle defects. We further determined that myocardial *Kmt2d* deletion led to decreased H3K4me1 and H3K4me2 at enhancers and promoters. Finally, we identified KMT2D-bound regions in cardiomyocytes, of which a subset was associated with decreased gene expression and decreased H3K4me2 in mutant hearts. This subset included genes related to ion transport, hypoxia-reoxygenation and cell cycle regulation, suggesting that KMT2D is important for these processes. Our findings indicate that KMT2D is essential for regulating cardiac gene expression during heart development primarily via H3K4 di-methylation.

KEY WORDS: KMT2D, MLL2, MLL4, ALR, Kabuki syndrome, H3K4 methylation, Heart development, Mouse

INTRODUCTION

During heart development genes are tightly regulated to ensure expression in specific cardiac tissues at the appropriate time. It has emerged that dynamic changes in chromatin structure are crucial in controlling cardiac gene expression, implicating several chromatin remodelers and histone-modifying enzymes in the regulation of heart development, although the precise role of many chromatin modifiers remains unknown (Chang and Bruneau, 2012).

H3K4 methylation is a histone modification linked to transcriptional activation. H3K4me1, along with H3K27Ac enrichment, is associated with active enhancers (Creyghton et al., 2010), and H3K4me3 is highly enriched at promoters (Lauberth et al., 2013), whereas H3K4me2 is enriched at enhancers, promoters and within the gene body (Bernstein et al., 2005; Pekowska et al., 2010). Each histone mark is associated with specific regulatory elements and functions, indicating a complex control of active gene transcription.

A study of *de novo* mutations in severe congenital heart defect (CHD) cases showed a significant over-representation of genes related to H3K4 methylation (Zaidi et al., 2013), highlighting the importance of this histone modification in heart development. In particular, mutations in the H3K4 methyltransferase *KMT2D* (also known as *MLL2*, *MLL4* and *ALR*) have been identified as a major cause of Kabuki syndrome, with ∼60% of patients diagnosed with CHDs, most frequently aortic coarctation, atrial and ventricular septal defects. Most *KMT2D* mutations are predicted to result in haploinsufficiency (Ng et al., 2010; Matsumoto and Niikawa, 2003), suggesting an important role for *KMT2D* in heart development (Digilio et al., 2001; Yuan, 2013; Ng et al., 2010).

KMT2D is a key regulator of gene expression in the context of cellular differentiation in diverse tissues. Hu et al. (2013), Guo et al. (2013) and Lee et al. (2013) showed reduced global H3K4me1 levels in a *KMT2C/D* (*MLL3/4*) double-knockout colon cancer cell line, and identified a majority of KMT2D binding sites located in putative enhancer elements. *Kmt2d* is essential for mouse adipogenesis, myogenesis, macrophage activation and lymphomagenesis, demonstrating additional roles for KMT2D as a mono- and di-methyltransferase at enhancers (Lee et al., 2013; Kaikkonen et al., 2013; Ortega-Molina et al., 2015). Collectively, these findings indicate that KMT2D regulates key gene expression programs via H3K4 mono- and di-methylation, and its role depends on cellular and temporal contexts.

In the present study, we identify KMT2D as an essential regulator of heart development. A single copy of *Kmt2d* is sufficient for normal heart development and leads to mild alterations in heart function. *Kmt2d* deletion in cardiac precursors and cardiomyocytes disrupts cardiogenesis. We show that *Kmt2d* deletion in these cardiac populations results in downregulation of ion transport and cell cycle genes, leading to altered calcium handling and cell cycle defects in cardiomyocytes. Myocardial deletion of *Kmt2d* leads to decreased H3K4me1 at H3K27Ac-enriched enhancers and decreased H3K4me2 at promoters and enhancers. Finally, we identify KMT2D binding regions in cardiomyocytes, of which a subset is associated with decreased gene expression and decreased H3K4me2 levels in mutant embryonic hearts. Our results indicate that KMT2D, through its primary role as an H3K4 di-methyltransferase, is required for regulating specific regulatory programs during heart development.

RESULTS

A single copy of *Kmt2d* is sufficient for normal heart development and leads to mild functional defects

Heart development relies on appropriate gene regulation in multiple cell types. We examined the expression of KMT2D in the

[1]Gladstone Institute of Cardiovascular Disease, San Francisco, CA 94158, USA. [2]Roddenberry Center for Stem Cell Biology and Medicine at Gladstone, San Francisco, CA 94158, USA. [3]Biomedical Sciences Graduate Program, University of California, San Francisco, San Francisco, CA 94158, USA. [4]National Institute of Diabetes and Digestive and Kidney Diseases, National Institutes of Health, Bethesda, MD 20892, USA. [5]Cardiovascular Research Institute, University of California, San Francisco, San Francisco, CA 94143, USA. [6]Department of Pediatrics, University of California, San Francisco, San Francisco, CA 94143, USA.
*Deceased

‡Author for correspondence (benoit.bruneau@gladstone.ucsf.edu)

Received 4 November 2015; Accepted 21 January 2016

Development (2016) 143, 810-821 doi:10.1242/dev.132688

developing embryonic mouse heart. Immunofluorescence for KMT2D on embryonic day (E) 9.5 to E12.5 cardiac sections showed ubiquitous expression in the developing heart (Fig. S1A). Closer examination of E12.5 hearts showed expression in both cardiomyocytes (Fig. 1A) and endocardial cells (Fig. 1B).

Kabuki syndrome patients carry truncating mutations in *KMT2D*, which are predicted to result in haploinsufficiency. To determine if *Kmt2d* is haploinsufficient in mice, mice carrying a floxed allele of *Kmt2d* (*Kmt2d*^{fl}, referred to as *Mll4*^{f} in Lee et al., 2013) were crossed to transgenic *ACTB-Cre* mice (Lewandoski et al., 1997) to generate mice heterozygous for a *Kmt2d*$^{\Delta}$ null allele. qRT-PCR confirmed depletion of the *Kmt2d* transcript by 50% in E8.0 *Kmt2d*$^{\Delta/+}$ embryos compared with control *Kmt2d*$^{+/+}$ littermates (Fig. 1C). *Kmt2d*$^{\Delta/+}$ mice survived to adulthood (Table S1). At postnatal day (P) 35, *Kmt2d*$^{\Delta/+}$ mice had normal heart weight/body weight (Fig. 1D), and no differences in cardiac morphology compared with littermate wild-type controls (Fig. 1E,F). To determine if *Kmt2d*$^{\Delta/+}$ mice had altered cardiac function, we performed echocardiography on P35 *Kmt2d*$^{\Delta/+}$ and wild-type controls. There were no significant changes in fractional shortening in *Kmt2d*$^{\Delta/+}$ mice (Fig. 1G), but measured a significant narrowing of the diameter of the ascending aorta (Fig. 1H) and increased aortic valve peak velocity (Fig. 1I).

We conclude that a single copy of *Kmt2d* is sufficient for normal mouse heart development and function, with mild defects in the ascending aorta.

Conditional deletion of *Kmt2d* in cardiac precursors and myocardium disrupts cardiac development

To determine if KMT2D is required for heart development, we interbred *Kmt2d*$^{\Delta/+}$ animals to obtain homozygous *Kmt2d*$^{\Delta/\Delta}$ embryos. No live *Kmt2d*$^{\Delta/\Delta}$ offspring were observed (Table S1), and *Kmt2d*$^{\Delta/\Delta}$ embryos at E8.0 lacked somites and headfolds (Fig. S2A). qRT-PCR confirmed depletion of *Kmt2d* in *Kmt2d*$^{\Delta/\Delta}$ mutants (Fig. S2B). Severe morphological defects in the *Kmt2d*$^{\Delta/\Delta}$ embryos indicated an early requirement of *Kmt2d* in embryogenesis, precluding assessment of its role during heart development. Therefore, we used conditional deletion of *Kmt2d* to investigate its role in specific cardiac populations (Fig. 2A).

We deleted *Kmt2d* using *Mesp1*^{Cre}, which is expressed in mesodermal precursors (Saga et al., 1999), and *Mef2cAHF::Cre*, which is expressed in anterior heart field (AHF) precursors (Verzi

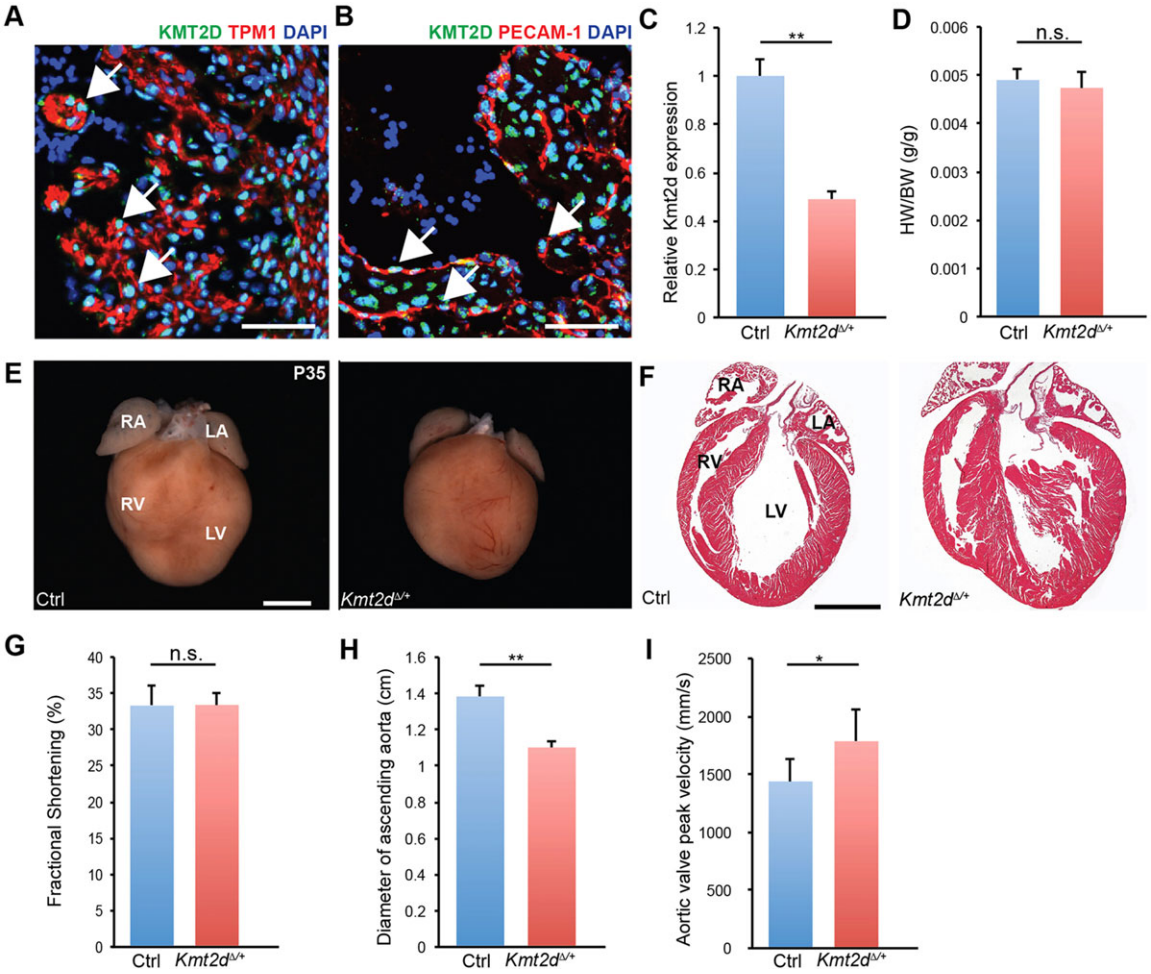

Fig. 1. *Kmt2d*$^{\Delta/+}$ mice have normal cardiac development but exhibit mild narrowing of the ascending aorta. (A,B) Magnified images of the left ventricle from a four-chamber view section at E12.5 shows (A) KMT2D expression (green) in the nuclei (DAPI, blue) of myocardial cells (TPM1, red) (arrows) and (B) KMT2D expression in the nuclei of endocardial cells (PECAM1, red) (arrows). (C) qRT-PCR for *Kmt2d* transcript levels in E8.0 control and *Kmt2d*$^{\Delta/+}$ embryos. (D) Heart weight to body weight ratio of P35 control (n=6) and *Kmt2d*$^{\Delta/+}$ (n=5) mice. (E) Representative images of P35 control and *Kmt2d*$^{\Delta/+}$ hearts. (F) Four-chamber view cardiac sections from P35 control and *Kmt2d*$^{\Delta/+}$ mice stained with Hematoxylin and Eosin (H&E). (G-I) Fractional shortening (G), diameter of the ascending aorta (H) and peak velocity of blood flow through the aortic valve (I) of P35 control and *Kmt2d*$^{\Delta/+}$ mice. RA, right atrium; LA, left atrium; RV, right ventricle; LV, left ventricle. *P<0.05, **P<0.01; n.s., no significant difference. Error bars indicate s.d. Scale bars: 50 µm in A,B; 2 mm in E; 500 µm in F.

Development (2016) 143, 810-821 doi:10.1242/dev.132688

et al., 2005) (Fig. 2A); *Mesp1*^{Cre} will delete the ubiquitously expressed *Kmt2d* broadly in E7.0 mesoderm, whereas *Mef2cAHF::Cre* will delete *Kmt2d* in a domain restricted to AHF precursors and pharyngeal arches (Devine et al., 2014; Saga et al., 1999; Verzi et al., 2005). qRT-PCR confirmed a significant decrease in *Kmt2d* transcripts in the hearts of E9.0 mesodermal deletion mutants

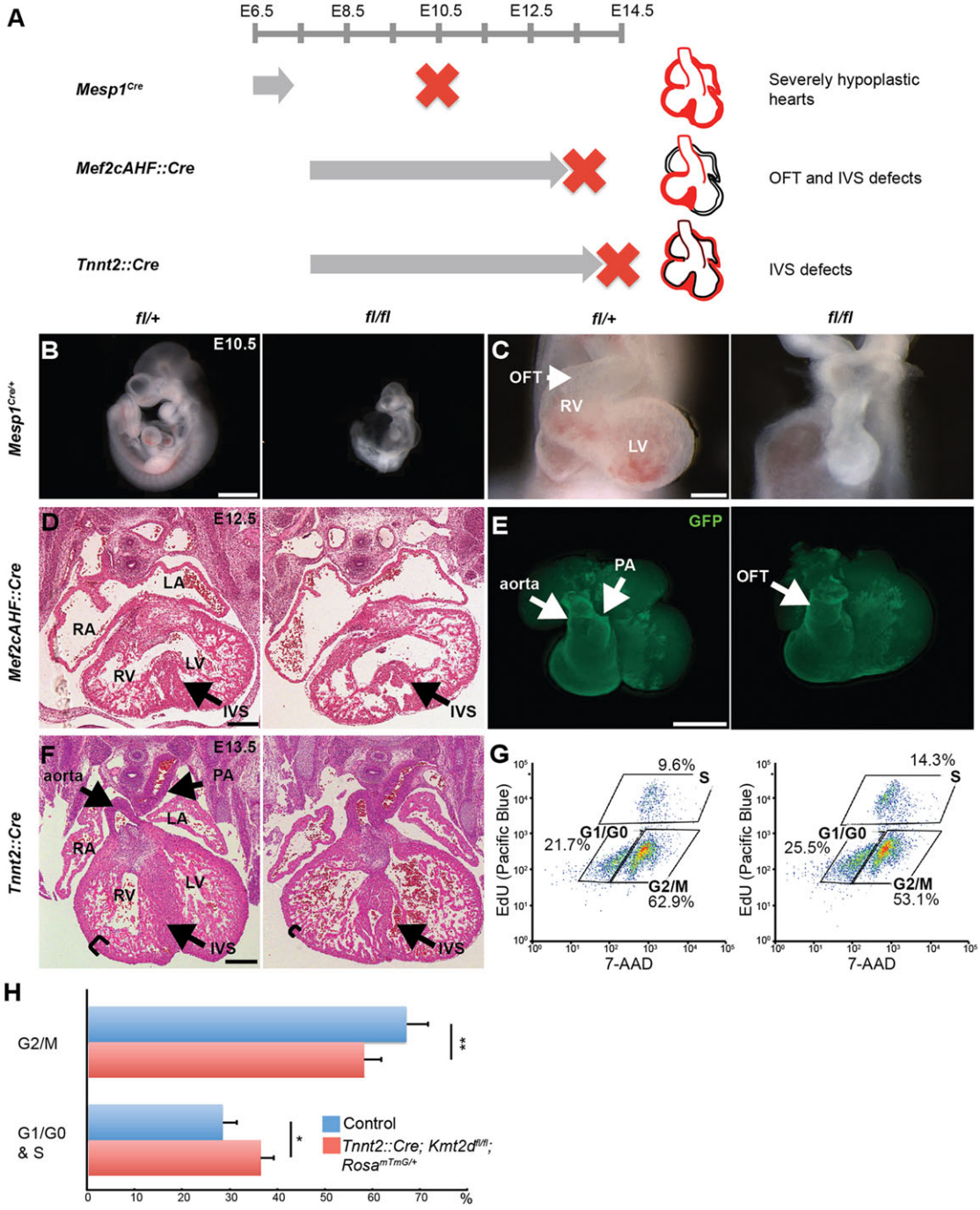

Fig. 2. Deletion of *Kmt2d* in cardiac precursors and myocardium leads to embryonic lethality and cardiac defects. (A) Schematic overview of *Kmt2d* deletion phenotypes in mesodermal precursors, anterior heart field (AHF) precursors and cardiomyocytes. (B) E10.5 *Mesp1*^{Cre}*;Kmt2d* $^{fl/fl}$ embryos show developmental delay compared with wild-type littermates. (C) E10.5 *Mesp1*^{Cre}*;Kmt2d* $^{fl/fl}$ mutants show severely hypoplastic hearts. (D) E12.5 *Mef2cAHF::Cre;Kmt2d* $^{fl/fl}$ four-chamber view cardiac sections stained with H&E show a disorganized interventricular septum (arrowheads). (E) E12.5 *Mef2cAHF::Cre;Kmt2d* $^{fl/fl}$*;Rosa*$^{mTmG/+}$ hearts show defects in outflow tract septation (arrowhead). GFP reporter is expressed in Cre-positive cells. (F) E13.5 *Tnnt2::Cre;Kmt2d* $^{fl/fl}$ four-chamber view cardiac sections stained with H&E show disorganized interventricular septum (arrowheads) and thin compact myocardium (brackets) in mutants. (G) E12.5 control (WT) and *Tnnt2::Cre;Kmt2d* $^{fl/fl}$*;Rosa*$^{mTmG/+}$ (cKO) hearts were labeled with EdU for newly synthesized DNA and EdU-labeled cells were detected with Pacific Blue azide using Click chemistry. Cells were stained with 7-AAD to determine total DNA content and cell cycle distribution was determined by FACS analysis, sorting for Cre-positive cells using GFP reporter. Representative FACS plots of the Cre-positive population show an increase in the number of cells in G1/G0 and S phase and a decrease in G2/M phase in the mutant. (H) Cell cycle analysis of E12.5 control and *Tnnt2::Cre;Kmt2d* $^{fl/fl}$*;Rosa*$^{mTmG/+}$ hearts (n=4 per genotype) shows an 8.0% increase in G1/G0 and S phases (P<0.05) and an 8.8% decrease in G2/M phases in mutants (P<0.01). RV, right ventricle; LV, left ventricle; PA, pulmonary artery; OFT, outflow tract; IVS, interventricular septum. *P<0.05, **P<0.01. Error bars indicate s.d. Scale bars: 1 mm in B; 200 µm in C; 250 µm in D,F; 500 µm in E.

Development (2016) 143, 810-821 doi:10.1242/dev.132688

(P<0.05, Fig. S2C) and E11.5 AHF deletion mutants (P<0.05, Fig. S2D) compared with heterozygous controls.

To verify that the Cre deletion leads to a loss of KMT2D protein, we used a Cre reporter allele, *Rosa*^{mTmG} (Muzumdar et al., 2007). Immunostaining of E10.5 *Mef2cAHF::Cre;Kmt2d*$^{fl/fl}$*;Rosa*$^{mTmG/+}$ hearts showed reduced KMT2D levels in Cre-deleted GFP^{+} cells (Fig. S2E).

No live *Mesp1*^{Cre}*;Kmt2d*$^{fl/fl}$ mutants were recovered after E10.5 (Table S2). E10.5 mutants appeared developmentally delayed, exhibiting pericardial edema and a linear heart tube (Fig. 2B,C). Similarly, no live *Mef2cAHF::Cre;Kmt2d*$^{fl/fl}$ offspring were observed. *Mef2cAHF::Cre;Kmt2d*$^{fl/fl}$ mice were found at Mendelian ratios until E11.5, and this decreased subsequently, with all mutants dying by E13.5 (Table S2). The gross morphology of E12.5 mutant embryos and hearts appeared normal (Fig. S2F,G). However, examination of histological sections of E12.5 mutant hearts revealed a disorganized interventricular septum (Fig. 2D). E12.5 mutant hearts showed a failure of outflow tract septation into the aorta and pulmonary artery (Fig. 2E, Fig. S2H). The cardiac defects of both genotypes indicated that *Kmt2d* is required in cardiac mesoderm and AHF precursors for heart development.

Since mesodermal and AHF precursors contribute to multiple cardiac cell types, we determined if *Kmt2d* was required in cardiomyocytes by deleting *Kmt2d* using *Tnnt2::Cre*, which is expressed in the embryonic myocardium from E7.5 onwards (Jiao et al., 2003). qRT-PCR confirmed a significant decrease of *Kmt2d* transcript in E11.5 mutant hearts, although the *Kmt2d* transcript was not completely lost, which was likely to be due to the contribution of non-myocyte populations such as endocardium and cardiac fibroblasts (P<0.05, Fig. S2I). *Tnnt2::Cre;Kmt2d*$^{fl/fl}$ embryos were found at Mendelian ratios until E13.5, but no live mutants were observed after E14.5 (Table S2). The gross morphology of E13.5 mutant embryos and hearts appeared normal (Fig. S2J,K). Examination of histological sections of E13.5 mutant hearts revealed thin compact myocardium and disorganized ventricular septum (Fig. 2F), similar to the AHF precursor deletion phenotype. However, myocardial deletion mutants showed normal septation of the outflow tract into the aorta and pulmonary artery.

Hypoplasia of the compact myocardium in *Tnnt2::Cre;Kmt2d*$^{fl/fl}$ mutants suggested decreased cardiomyocyte proliferation. To test this hypothesis, we performed cell cycle analysis on E12.5 control and mutant hearts (n=4 for each genotype). Cell cycle distribution was determined by EdU and 7-AAD double staining, sorting for Cre-positive cells with GFP fluorescence (Fig. 2G). In controls, 66.9% of the Cre-positive cell population was in the G2/M phase, which decreased to 58.0% in the mutants. In controls, 28.3% of the Cre-positive cell population was in the G1/G0 and S phases, which increased to 36.3% in the mutants. The cell population in the G1/G0 and S phases also increased from 28.3% to 36.3% (Fig. 2H). This indicated that a portion of cells is arrested in the G1/G0 and S phases, which could contribute to hypoplasia of the compact myocardium.

These results indicate that *Kmt2d* is required in cardiac precursors and myocardium during heart development, with distinct phenotypes suggesting that *Kmt2d* plays specific roles in each cardiac population.

Loss of *Kmt2d* leads to downregulation of ion transport genes and altered calcium handling in ventricular myocytes

To assess the transcriptional consequences of *Kmt2d* loss during heart development, we performed global gene expression analyses of embryonic hearts. To avoid confounding secondary effects, we obtained embryonic hearts at the developmental stages when the earliest cardiac defects were observed. For *Mesp1*^{Cre} crosses, we used E9.0 hearts (n=4 per genotype). For *Mef2cAHF::Cre*, we used E11.5 right ventricles and outflow tracts (n=3 per genotype), which are the regions where *Kmt2d* is deleted. For *Tnnt2::Cre* crosses, we used E11.5 embryonic hearts (n=3 per genotype).

At a false discovery rate (FDR) <0.05, we found 2226 genes dysregulated in *Mesp1*^{Cre} mutants, 1212 genes dysregulated in *Mef2cAHF::Cre* mutants and 774 genes dysregulated in *Tnnt2::Cre* mutants (Fig. 3A, Table S3). Average-linkage cluster analysis showed that differentially expressed genes in *Mesp1*^{Cre}, *Mef2cAHF::Cre* and *Tnnt2::Cre* mutants mostly clustered separately, with some overlap (Fig. 3A), indicating that *Kmt2d* regulates distinct subsets of genes in each cardiac population. Gene ontology (GO) analysis revealed that the distinct subsets of genes upregulated in the three deletion mutants were enriched for functions in hypoxia response, whereas downregulated genes were enriched for functions in ion transport and homeostasis (Fig. 3A). Downregulation of genes related to ion transport, such as *Atp1a2*, *Snta1*, *Camk2a* and *Fxyd1*, were validated by qRT-PCR in *Tnnt2::Cre;Kmt2d*$^{fl/fl}$ deletion mutants (Fig. S3A).

To determine biological functions commonly dysregulated in all three cardiac deletion mutants, we analyzed this dataset using Ingenuity pathway analysis (IPA). Predicted disease associations included heart failure and myocardial infarction (Fig. 3B), suggesting strong disruption of cardiac function and circulatory failure. We observed that common dysregulated canonical pathways included calcium signaling, hypoxia signaling and G1/S cell cycle checkpoint regulation (Fig. 3C). In addition, common dysregulated biological functions included anemia, muscle contractility, ion homeostasis and reactive oxygen species (ROS) (Fig. S3B). We also observed that the predicted dysregulation of upstream regulators included multiple hypoxia response genes, such as *Hif1a* and *Commd1* (Fig. S3C). We analyzed the *Tnnt2::Cre* deletion gene expression dataset further using an unbiased gene set enrichment analysis (GSEA) (Subramanian et al., 2005). Similarly, we observed a significant decrease in inorganic anion transport genes and erythropoietic markers, as well as an enrichment of hypoxia response genes (FDR<0.01, Fig. S3D-F).

To determine if the decrease in ion transport gene expression led to a loss of protein expression, we examined the expression of ATP1A2, the alpha-2 isoform of the Na^{+},K^{+}-ATPase, in *Tnnt2::Cre;Kmt2d*$^{fl/fl}$ and control hearts. In the left atria and interventricular septum, ATP1A2 was decreased in Cre-positive mutant cardiomyocytes (Fig. S4A,B). By contrast, HIF1A, a key hypoxia response factor, was detected predominantly in Cre-negative cells (Fig. S4C), suggesting that the increase in hypoxic response gene expression might be a secondary response.

In the myocardial deletion mutants, downregulated ion transport genes included *Snta1* and *Fxyd1*. SNTA1 associates with the cardiac sodium channel SCN5A and the plasma membrane Ca^{2+}-ATPase PMCA4B (also known as ATP2B4), and mutations in *SNTA1* are associated with long QT syndrome 12 (Ueda et al., 2008). *Fxyd1* encodes a sarcolemmal protein (also known as phospholemman) that regulates the ion channels Na^{+},K^{+}-ATPase and sodium-calcium exchanger NCX1 (also known as SLC8A1), and thus exerts effects on intracellular Ca^{2+} concentration. *Fxyd1*-deficient cardiomyocytes have increased Na^{+}/Ca^{2+} exchange current (Zhang et al., 2006), which is associated with increased action potential (AP) duration. These studies suggest downregulation of *Snta1* and *Fxyd1* might lead to altered intracellular calcium levels ($[Ca^{2+}]_i$) in cardiomyocytes.

Development (2016) 143, 810-821 doi:10.1242/dev.132688

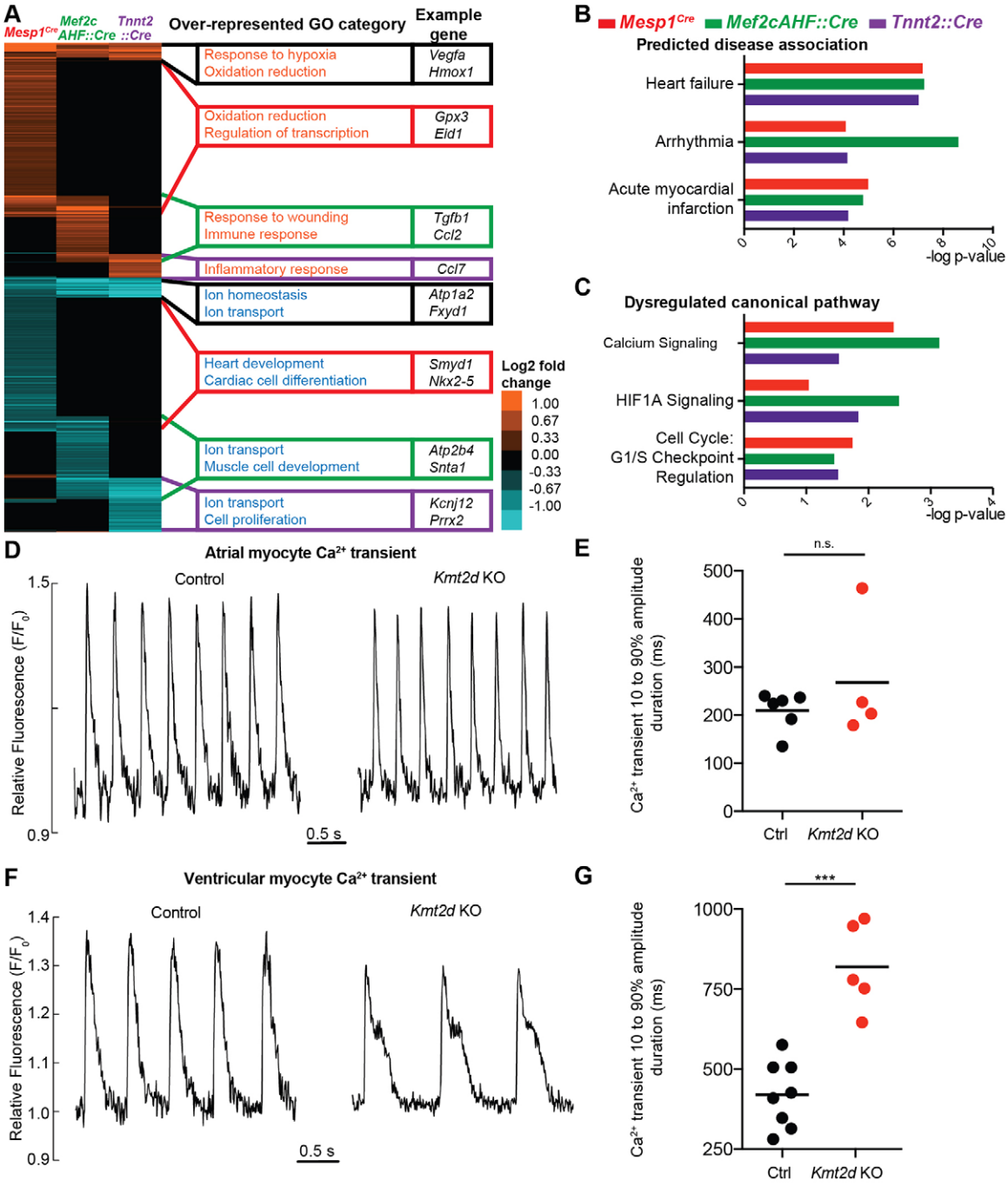

Fig. 3. Deletion of *Kmt2d* in cardiac precursors and myocardium leads to downregulation of ion transport genes and altered calcium handling in ventricular cardiomyocytes. (A) RNA-Seq analysis comparing differentially expressed genes in E9.0 *Mesp1*^{Cre}*;Kmt2d*$^{fl/fl}$ mutant hearts, E11.5 *Mef2cAHF::Cre; Kmt2d*$^{fl/fl}$ right ventricles and outflow tract and E11.5 *Tnnt2::Cre;Kmt2d*$^{fl/fl}$ mutant hearts (FDR<0.05). (B) IPA of differentially expressed genes in all three deletion genotypes shows that common disease associations that were significantly predicted are related to heart failure (P<0.05). (C) IPA shows that common canonical pathways that were significantly dysregulated are associated with calcium signaling, HIF1A signaling and G1/S cell cycle checkpoint regulation (P<0.05). (D) Representative Fluo-4 fluorescence recordings from control and *Tnnt2::Cre;Kmt2d*$^{fl/fl}$ (*Kmt2d* KO) atrial myocytes isolated at E11.5. (E) Mean durations of Ca^{2+}-dependent Fluo-4 fluorescence transients plotted for control and *Kmt2d* KO atrial myocytes. Each point represents the Ca^{2+} transient duration from myocytes representing one embryonic heart, as determined at the level between 10% of the upstroke and 90% of the decay. An average of 5.8 samples (cells or clusters) were combined per point. n.s., no significant difference. (F) Representative Fluo-4 fluorescence recordings (upper panel) from control and *Kmt2d* KO ventricular myocytes isolated at E11.5. Typically, the Ca^{2+} transients, expressed relative to diastolic fluorescence (F_0), showed similar peak amplitudes but strong differences in duration due to the presence of a late shoulder or plateau in the *Kmt2d* KO myocytes. (G) Mean durations of Ca^{2+}-dependent Fluo-4 fluorescence transients plotted for control and *Kmt2d* KO ventricular myocytes. An average of 23 samples (cells or clusters) were combined per point. *Kmt2d* KO ventricular myocytes had a significantly prolonged duration at 819±137 ms (n=5) compared with controls at 420±103 ms (n=8) (***P<0.001).

Accordingly, we measured spontaneous $[Ca^{2+}]_i$ transients in E11.5 atrial and ventricular myocytes from mutants and controls to ascertain whether myocardial deletion of *Kmt2d* leads to altered Ca^{2+} handling. In atrial myocytes, mutant $[Ca^{2+}]_i$ transient waveforms were similar to those of controls (Fig. 3D) and the mean duration, measured at the level delimited by 10% of the initial

Development (2016) 143, 810-821 doi:10.1242/dev.132688

rise and 90% of the final decay, showed no significant differences between the genotypes (Fig. 3E). However, in the ventricular myocytes, mutant $[Ca^{2+}]_i$ transients exhibited prolonged waveforms (Fig. 3F), reflecting a prolonged AP duration (Fig. S4D). The mean duration was 819±137 ms (n=5) in mutants, approximately double that of controls (420±103 ms, n=8) (P<0.001, Fig. 3G), indicating a specific role for *Kmt2d* in regulating calcium handling in the ventricular myocardium. Because we performed RNA-Seq on whole hearts, we were not able to discern which dysregulated ventricular genes were primarily responsible for the electrophysiological abnormalities.

We conclude that *Kmt2d* regulates distinct subsets of genes in mesodermal precursors, AHF precursors and cardiomyocytes, but also generally controls the ion transport gene expression response. Reduced ion transport gene expression is likely to lead to prolonged Ca^{2+} transient duration in mutant ventricular myocytes, which reflects prolonged AP duration that might predispose mutants to arrhythmias.

Myocardial deletion of *Kmt2d* results in decreased H3K4me1 and H3K4me2 at enhancers and promoters

Since *Kmt2d* encodes an H3K4 methyltransferase, we sought to determine if myocardial deletion of *Kmt2d* leads to changes in H3K4 methylation levels. Western blot analysis did not show any decrease in the bulk levels of H3K4me1, H3K4me2 or H3K4me3 (Fig. S5A). To determine if there was a decrease in H3K4 methylation at specific genomic loci, we performed chromatin immunoprecipitation coupled with sequencing (ChIP-Seq) for H3K4me1, H3K4me2 and H3K4me3 on E11.5 control and mutant hearts (n=90 for each genotype). Hearts from each genotype were pooled to give three biological replicates, and we analyzed the data in conjunction with H3K27Ac ChIP-Seq data from wild-type E11.5 hearts (Nord et al., 2013). We then examined the enrichment of the histone methylation marks at the transcription start site (TSS) and non-TSS H3K27Ac-enriched sites, which marks active enhancers.

Average Metagene profile plots revealed a statistically significant decrease in H3K4me2 levels at the TSS and at non-TSS H3K27Ac-enriched sites in the *Tnnt2::Cre;Kmt2d* $^{fl/fl}$ mutant (Fig. 4A, blue and red lines). However, there were no significant changes in the levels of H3K4me1 and H3K4me3 at the TSS. Similarly, at non-TSS H3K27Ac-enriched sites, there were no changes in H3K4me3 levels, although there was a modest decrease in H3K4me1 levels.

We further examined average profile plots for the 492 genes that were downregulated in the myocardial deletion mutants. We observed a marked decrease in mutant H3K4me2 at the TSS and non-TSS H3K27Ac-enriched sites, with less noticeable differences in H3K4me1 and H3K4me3 (Fig. 4A, green and orange lines). This is similar to the global pattern, although this subset of 492 genes has higher average levels of H3K4me1 and H3K4me2 at both the TSS and non-TSS H3K27Ac-enriched sites compared with the global average.

We called 358,833 total merged peaks across all replicates of H3K4me1, H3K4me2 and H3K4me3. From these regions, we identified 2730 (0.8%) with decreased H3K4me1 (FDR<0.1) and 6417 (1.8%) with decreased H3K4me2 (FDR<0.1, Table S3), mapping to 2473 and 6573 genes, respectively. This indicates that only a subset of genomic loci had decreased H3K4me1 and H3K4me2. Most of the regions with decreased H3K4me1 were located at distal regulatory elements (Fig. S5B), similar to the global H3K4me1 enrichment (Table S4). By contrast, 54.2% of decreased H3K4me2 region-gene associations were proximal to a TSS, whereas 45.8% were located distal to a TSS (Fig. S5C). This indicates an approximately equal distribution of regions with decreased H3K4me2 at proximal and distal regulatory elements, whereas the global H3K4me2 enrichment is mostly at distal regulatory elements (88.7%, Table S4).

Of 492 genes downregulated in myocardial deletion mutants, 78 (15.9%) had decreased H3K4me1 levels (Fig. 4B) and 162 (32.9%) had decreased H3K4me2 levels (Fig. 4C), with enrichment of ion transport-related genes in these subsets (P<0.05). Compared with all downregulated genes, this enrichment in ion transport function is greater than expected for downregulated genes with decreased H3K4me2 (P=0.025), but not decreased H3K4me1 (P=0.22) (Table S5). The majority of genes with decreased H3K4me1 (2395 genes, 96.8%) and decreased H3K4me2 (6413 genes, 97.6%) did not show changes in gene expression, suggesting that a decrease in H3K4me1 or H3K4me2 levels is not sufficient for a decrease in gene expression and might require crosstalk with other mechanisms regulating transcription. It is possible that decreased H3K4me1 and H3K4me2 levels may be due to indirect effects. However, we might also fail to detect many regions with decreased H3K4 methylation levels in cardiomyocytes by examining embryonic hearts with heterogeneous cell populations. Nonetheless, we find that, compared with all expressed genes with decreased H3K4 methylation, downregulated genes are significantly more likely to be associated with decreased H3K4me1 regions (P=0.025) and decreased H3K4me2 regions (P=0.054) (Table S6).

Interestingly, only 168 regions have reductions in both H3K4me1 and H3K4me2 levels, corresponding to 6.2% of regions with decreased H3K4me1 or 2.6% of regions with decreased H3K4me2 (Fig. 4D). Of these 168 regions, only seven mapped to downregulated genes, suggesting that KMT2D has distinct roles in maintaining H3K4me1 and H3K4me2 levels at different genomic regions. No decrease in H3K4me1 and H3K4me3 levels was observed at the TSS of *E2f2* despite a substantial decrease in H3K4me2 levels (Fig. S5D), further illustrating that KMT2D is highly specific in regulating H3K4me1 and H3K4me2 levels at these genomic loci in the embryonic heart.

KMT2D binds to genomic regions associated with cell cycle, hypoxia-reoxygenation and ion transport genes in cardiomyocytes

To determine if KMT2D localizes to genomic regions to directly maintain H3K4me2 levels, we performed ChIP-Exo for KMT2D. Since E11.5 hearts had limited cell numbers, we used cardiomyocytes derived from embryonic stem cells (ESCs) (Wamstad et al., 2012). To validate the use of ESC-derived cardiomyocytes, we compared H3K4me1 and H3K4me3 enrichment in E11.5 hearts, ESC-derived cardiomyocytes, and ESCs; this demonstrated strong correlations in H3K4 methylation profiles between E11.5 hearts and differentiated cardiomyocytes, distinct from the ESC profiles (Fig. S6A).

We identified 6747 genomic regions bound by KMT2D (Table S3), which mapped to 4880 genes. 23.1% of region-gene associations were located within 5 kb of the TSS, whereas 76.9% were located 5 to 100 kb from the TSS (Fig. 5A). Thus, most KMT2D binding localizes to distal regulatory regions.

We examined KMT2D-bound regions and found that GO categories such as heart development and cell proliferation were over-represented (Fig. 5B). Motif analysis of the KMT2D-bound regions revealed enrichment of motifs matching transcription factors with crucial functions in cardiac development (Fig. S6B), including HIF1A, MYC, SP3, TEAD1 and SRF (Iyer et al., 1998;

Development (2016) 143, 810-821 doi:10.1242/dev.132688

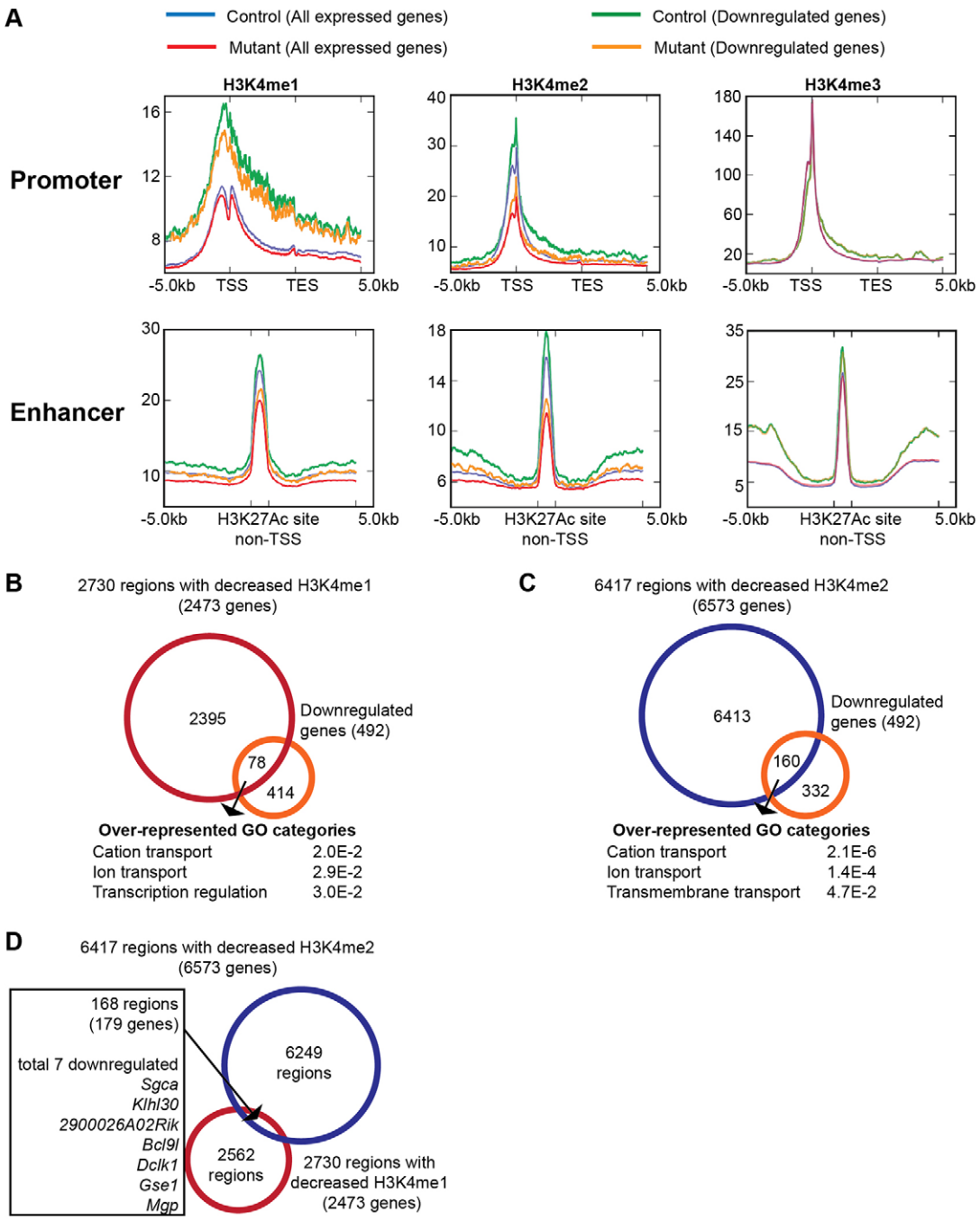

Fig. 4. Myocardial deletion of *Kmt2d* results in a decrease in average H3K4me1 and H3K4me2 levels at enhancers and promoters. (A) Metagene profiles showing the average distribution of H3K4me1, H3K4me2 and H3K4me3 input-normalized tag density at promoters and enhancers in E11.5 control and *Tnnt2::Cre;Kmt2d* $^{fl/fl}$ hearts. For all expressed genes and 492 downregulated genes analyzed, mutants show decreased H3K4me1 levels at enhancers, decreased H3K4me2 levels at promoters and enhancers, and no difference in H3K4me3 levels. (B) 2730 regions with decreased H3K4me1 levels (FDR<0.1) are assigned to 2473 genes by proximity using Stanford GREAT. GO categories of 78 downregulated genes with decreased H3K4me1 in mutant hearts are over-represented for ion transport genes. (C) 6417 regions with decreased H3K4me2 levels (FDR<0.1) are assigned to 6573 genes by proximity using GREAT. GO categories of 162 downregulated genes with decreased H3K4me2 are over-represented for ion transport genes. (D) Venn diagram representing the overlap of 2730 regions with decreased H3K4me1 with 6417 regions with decreased H3K4me2. Of the overlapping 168 regions mapped to 179 genes, only seven genes are downregulated in E11.5 *Tnnt2::Cre;Kmt2d* $^{fl/fl}$ hearts. TSS, transcription start site; TES, transcription end site.

Moens et al., 1993; van Loo et al., 2007; He et al., 2011; Parlakian et al., 2004). This suggests that the KMT2D methyltransferase complex may be recruited by these transcription factors. We further examined these KMT2D-bound regions for changes in H3K4 methylation in E11.5 hearts; although this comparison is not ideal owing to the different cellular origins and the heterogeneity of the E11.5 heart, the comparison yielded significant results. Similar to the trend observed in all expressed genes, we observed a greater decrease in H3K4me2 levels than H3K4me1 levels, and no change in H3K4me3 levels (Fig. S6C), suggesting that KMT2D is required at specific genomic loci to maintain H3K4me1 and H3K4me2 levels.

Development (2016) 143, 810-821 doi:10.1242/dev.132688

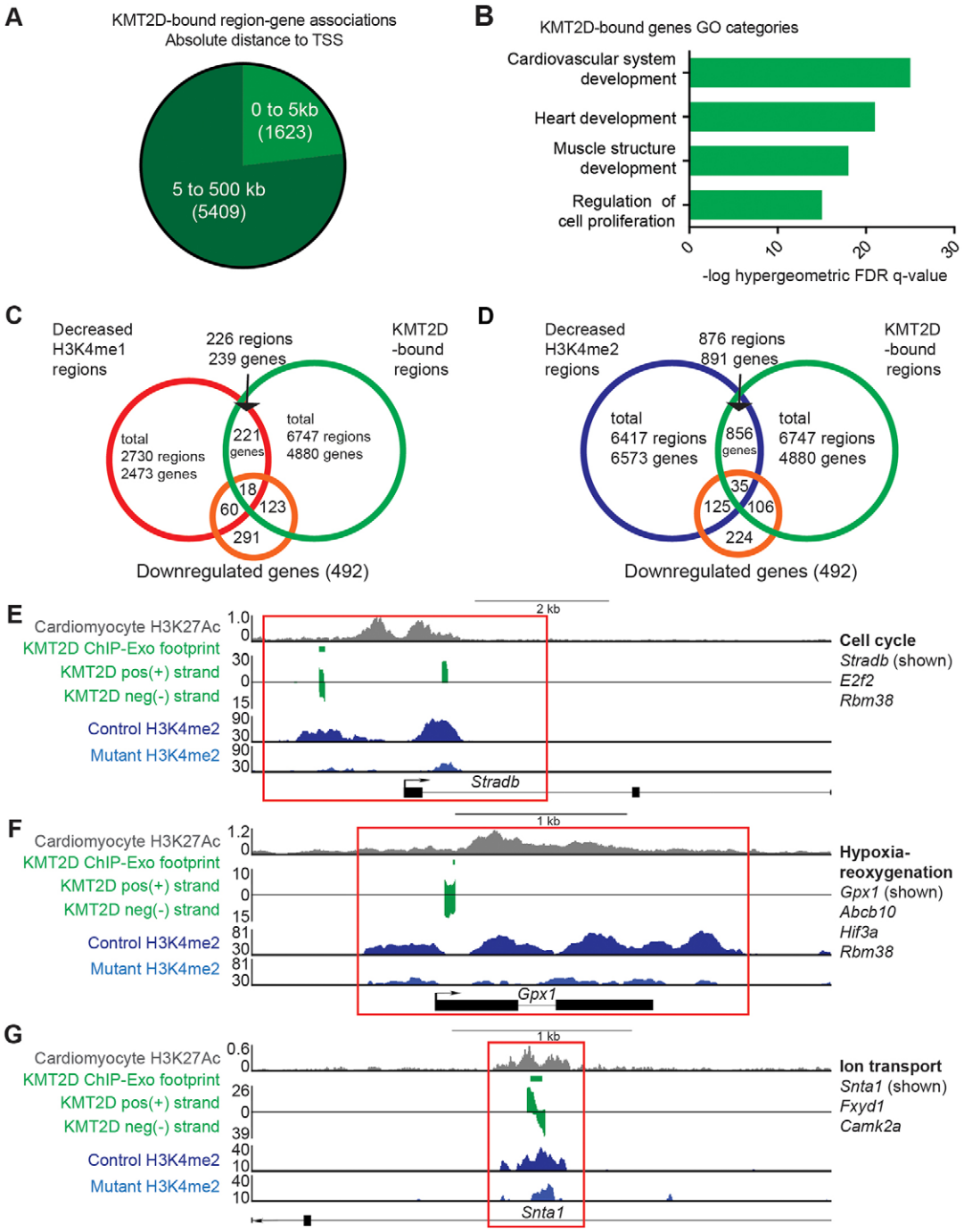

Fig. 5. KMT2D binds to promoter and enhancer regions of genes related to cell cycle, hypoxia-reoxygenation and ion transport. (A) 6747 regions bound by KMT2D in *in vitro* cardiomyocytes are assigned to 4880 genes by proximity using Stanford GREAT. 1623 region-gene associations are within 5 kb of a TSS and 5409 region-gene associations are 5 to 100 kb of a TSS. (B) GO categories of KMT2D-bound genes are over-represented for heart development and cell proliferation. (C) Venn diagram showing that only a subset of 18 genes overlap between 492 downregulated genes in E11.5 *Tnnt2::Cre;Kmt2d*$^{fl/fl}$ hearts and regions bound by KMT2D with decreased H3K4me1 levels (FDR<0.1). (D) Venn diagram showing that only a subset of 35 genes overlap between 492 downregulated genes in E11.5 *Tnnt2::Cre;Kmt2d*$^{fl/fl}$ hearts and regions bound by KMT2D with decreased H3K4me2 levels (FDR<0.1). (E) Representative browser tracks of KMT2D ChIP-Exo positive strand, negative strand, and resulting footprint shows that KMT2D binds to the TSS of the cell cycle gene *Stradb* in cardiomyocytes, which corresponds to a region with decreased H3K4me2 (FDR<0.1) in mutant hearts (red box). (F) KMT2D binds to the TSS of the antioxidant enzyme gene *Gpx1* in cardiomyocytes, which corresponds to a region with decreased H3K4me2 (FDR<0.1) in mutant hearts (red box). (G) KMT2D binds to the intronic H3K27Ac-enriched enhancer of the ion transport gene *Snta1* in *in vitro* cardiomyocytes, which corresponds to a region with decreased H3K4me2 (FDR<0.1) in mutant hearts (red box). The H3K27Ac browser track *y*-axis corresponds to reads per million; for the other tracks the *y*-axis corresponds to input-normalized tag density.

Finally, we investigated which KMT2D direct targets require KMT2D to maintain H3K4me2 levels and gene expression. We found that a small percentage of KMT2D-bound regions (3.4%, 226 regions corresponding to 239 genes) exhibited decreased H3K4me1 levels in E11.5 myocardial deletion mutant hearts, and a subset of 18 genes showed a concomitant decrease in gene expression

Development (2016) 143, 810-821 doi:10.1242/dev.132688

(Fig. 5C; Table S7). There were no enriched functions for this subset of 18 genes. Since E11.5 hearts have a heterogeneous cell population including non-myocytes, the overlap between KMT2D-bound genes and genes with decreased H3K4 methylation levels might be under-represented. We have further examined KMT2D-bound regions with decreased H3K4me2 (13%, 876 regions corresponding to 891 genes) and found greater overlap with downregulated genes (35 genes, Fig. 5D; Table S7).

In this subset of 35 genes, which represents KMT2D direct targets in cardiomyocytes that require KMT2D for normal H3K4me2 levels and gene expression in E11.5 hearts, we identified genes related to cell cycle, hypoxia-reoxygenation and ion transport. This includes *Stradb* (Fig. 5E), which encodes a pseudokinase implicated in G1 phase cell cycle arrest (Boudeau et al., 2006), and *Gpx1* (Fig. 5F), which encodes an antioxidant enzyme that protects cardiac mitochondria against reoxygenation-induced ROS (Thu et al., 2010). The subset also included the ion transport genes *Snta1* and *Fxyd1* (Fig. 5G), which suggests that the electrophysiological defects observed in *Kmt2d*-deficient cardiomyocytes might be due to direct KMT2D regulation of ion transport gene expression via H3K4 di-methylation.

DISCUSSION

We identified an essential role for KMT2D as a regulator of heart development. Our work demonstrates that *Kmt2d* is required in cardiac precursors and cardiomyocytes during cardiogenesis, with distinct phenotypes and dysregulated genes that suggest *Kmt2d* plays specific roles in each cardiac population. In the absence of *Kmt2d*, ion transport genes are downregulated in embryonic hearts, with a corresponding cellular phenotype with altered calcium handling. We further show that KMT2D is required for H3K4 mono- and di-methylation at promoters and enhancers of a subset of genes. In particular, we identified the requirement for KMT2D for H3K4 di-methylation at several genes related to ion transport, hypoxia-reoxygenation and cell cycle. Taken together, our findings suggest that KMT2D acts primarily as an H3K4 di-methyltransferase to regulate a specific cardiac transcriptional program for ion homeostasis and heart development (Fig. 6).

KMT2D is required for H3K4 mono- and di-methylation at enhancers and promoters

Most studies have focused on the association of H3K4me1 with enhancers and H3K4me3 with promoters of actively transcribed genes, but less is understood about the dynamics of H3K4me2 distribution and its contribution to gene expression (Ruthenburg et al., 2007; Shilatifard, 2012). Previous work identified H3K4me2 enrichment at enhancers, defining lineage-specific recruitment sites on chromatin (Lupien et al., 2008; Ong and Corces, 2011). H3K4me2 is also enriched in genomic regions surrounding the TSS of tissue-specific genes, with dynamic distribution during cell differentiation and development, suggesting that H3K4me2 enrichment at promoter regions plays a key role in regulating tissue-specific gene expression (Pekowska et al., 2010; Zhang et al., 2012; Popova et al., 2012).

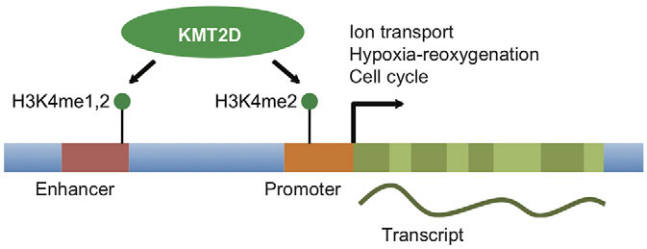

Fig. 6. KMT2D is required for H3K4 di-methylation (and mono-methylation) to maintain specific gene expression programs in heart development. Diagrammatic representation of a protein-coding gene, including promoter and enhancer, acted upon by KMT2D to deposit the histone modifications H3K4me1 and H3K4me3.

Studies in mammalian cells have uncovered the role of KMT2D as an H3K4 mono- and di-methyltransferase at enhancer or promoter regions (Hu et al., 2013; Guo et al., 2013; Lee et al., 2013; Kaikkonen et al., 2013; Ortega-Molina et al., 2015; Zhang et al., 2015). In agreement with these studies, we identified KMT2D-bound regions at both promoters and enhancers of cardiac genes. In the absence of *Kmt2d*, we observe that a subset of these genes is downregulated, with a corresponding decrease in H3K4me2 levels at enhancers or promoters and gene bodies at KMT2D-bound regions. We also observe a decrease in H3K4me1 levels at a smaller subset of enhancer regions, which are distinct from regions with decreased H3K4me2 levels. Our results suggest that KMT2D is an H3K4 mono- and di-methyltransferase required both at enhancers and promoters for active gene expression, with a specific role for KMT2D as an H3K4 di-methyltransferase at promoters. It will be important in future studies to gain a better understanding of the significance of specific H3K4 di-methylation distribution at promoters or enhancers for transcription activation.

Although we observed several thousand genomic regions with decreased H3K4me2 or H3K4me1, only a small subset of genes within these groups was downregulated. This suggests that not all genes are sensitive to a loss in H3K4me1 or H3K4me2 levels. There might be a temporal delay in H3K4me1- or H3K4me2-dependent gene expression, or some genes are downregulated at a later developmental stage. Alternately, changes in H3K4me1 or H3K4me2 levels alone might not effect a direct change in gene expression. Further studies of genetic interactions between *Kmt2d* and other histone modifiers might provide additional insight into histone crosstalk and the epigenetic regulation of gene expression.

KMT2D regulates cardiac gene expression related to ion transport, hypoxia-reoxygenation and the cell cycle

We found that myocardial deletion of *Kmt2d* leads to changes in ion transport gene expression and altered calcium handling in ventricular myocytes, indicating a role for KMT2D in regulating ion homeostasis. A similar observation has been made for adult cardiomyocyte deletion of *Paxip1*, which encodes a KMT2D complex-specific subunit, leading to changes in ion channel gene expression and arrhythmias (Stein et al., 2011). Furthermore, a child with severe Kabuki syndrome was reported to have bradycardia and asystole (Shah et al., 2005). These data suggest that the KMT2D complex has an important role in regulating cardiac electrophysiology.

Functional ion channel activity is crucial in the embryonic heart, particularly during mid-gestation. In rats treated during gestation, teratogenic doses of potassium channel blockers increased embryonic death associated with a significantly increased incidence of cardiac defects, particularly ventricular septal defects and great vessel abnormalities, similar to what we observed in *Kmt2d* mutants (Webster et al., 1996; Abela et al., 2010). The channel-blocking drugs induce cardiac arrhythmia and heart failure in the embryos, leading to chronic hypoxia-reoxygenation damage, thus adversely affecting cardiogenesis and resulting in cardiac malformations (Wellfelt et al., 1999; Danielsson et al., 2001, 2007; Sköld et al., 2001). Our results are consistent with this observation, as *Kmt2d* mutants exhibit downregulation of ion transport genes and

Development (2016) 143, 810-821 doi:10.1242/dev.132688

concomitant upregulation of hypoxia response genes. This suggests that disruption of ion channel activity due to *Kmt2d* deletion could contribute to the cardiac defects observed in mutants.

We also identified potential KMT2D target genes that might protect the heart from hypoxia-reoxygenation damage. GPX1 and ABCB10 protect cardiac mitochondria against hypoxia-reoxygenation-induced oxidative stress, whereas HIF3A and RBM38 are negative regulators of HIF1A (Thu et al., 2010; Bayeva et al., 2013; Forristal et al., 2010; Cho et al., 2015). Cardiac mitochondria respond to hypoxia by increasing the generation of ROS, subjecting the heart to oxidative stress (Duranteau et al., 1998). This suggests that decreased expression of these genes could exacerbate hypoxia-reoxygenation injury in mutant hearts. *Stradb*, *E2f2* and *Rbm38* are important for cell cycle decisions between G0/G1 and S phase (Boudeau et al., 2006; Infante et al., 2008; Miyamoto et al., 2009), suggesting that the cell cycle defects that we observed in myocardial deletion mutants could be due to dysregulation of these genes.

It is likely that the mutant cardiac phenotypes are the combined result of multiple dysregulated KMT2D target genes. To better understand how KMT2D regulates heart development, it will be important to examine how KMT2D target genes interact during cardiogenesis and to determine the cardiac transcription factors that recruit the KMT2D complex for cell type-specific gene expression. Although Kabuki syndrome is a haploinsufficient, multi-organ syndrome in humans, our studies in cardiac-specific knockouts shed light on the primary nature of cardiac defects in the absence of KMT2D and uncover possible etiologies for CHDs in Kabuki syndrome patients.

In conclusion, we have discovered important and novel roles for *Kmt2d* in H3K4 mono- and di-methylation during heart development. Our work adds to the understanding of the transcriptional regulation of cardiac gene expression during heart development and highlights the contribution of histone modifiers. In future work, it will be important to understand how the distribution and dynamics of H3K4 mono- and di-methylation might interact with other transcriptional signals to drive transcription activation. It will also be important to establish whether KMT2D regulates ion homeostasis in other organ systems, and thus identify potential therapies for the multiple congenital anomalies observed in Kabuki syndrome.

MATERIALS AND METHODS

Mice

Kmt2d$^{fl/fl}$ [referred to as *Mll4*$^{f/f}$ in Lee et al. (2013)], *ACTB::Cre* (Lewandoski et al., 1997), *Mesp1*^{Cre} (Saga et al., 1999), *Mef2cAHF::Cre* (Verzi et al., 2005), *Rosa*^{mTmG} (Muzumdar et al., 2007), *Tnnt2::Cre* (Jiao et al., 2003) and *Tie2::Cre* (Kisanuki et al., 2001) mice have been described previously. These mice were backcrossed for at least five generations to a C57BL/6 background. Animals were treated in accordance with the guidelines of the University of California, San Francisco (UCSF) Institutional Animal Care and Use Committee (IACUC). Conceptuses were generated from timed matings and detection of the vaginal plug was considered as E0.5.

Echocardiography

Echocardiograms to assess systolic function were performed using the Vevo 770 High-Resolution Micro-Imaging System (VisualSonics). M-mode and two-dimensional measurements were made as described previously (Li et al., 2012). The measurements were made from five *Kmt2d*$^{\Delta/+}$ heterozygous mutants (n=5) and six wild-type control littermates (n=6).

Immunofluorescence and western blotting

Embryonic trunk regions were dissected out and fixed in 4% paraformaldehyde for 30 min, followed by serial incubations in 10%, 20% and 30% sucrose, then frozen in Tissue-Tek OCT Compound (Sakura Finetek). Cryosections (8 µm) were mounted on glass slides, dried for 20 min at room temperature, washed with PBS containing 0.1% Tween-20 (PBST) and incubated in blocking buffer (0.1 M Tris HCl pH 7.5, 0.15 M NaCl, 0.5% blocking reagent; PerkinElmer) for 1 h. Samples were incubated with primary antibodies at 4°C overnight in blocking buffer, washed with PBST and incubated with secondary antibodies for 1 h. Slides were then washed, stained with 1 µg/µl DAPI and mounted in Prolong Gold Antifade (Life Technologies). Whole-mount immunostaining of E12.5 hearts is described in the supplementary Materials and Methods. Western blotting was performed using standard techniques. Antibodies are listed in Table S8.

Cell cycle analysis

200 µl 5 mg/ml 5-ethnyl-2′-deoxyuridine (EdU) in PBS was injected per 8-week-old female mouse. After 2 h, E12.5 whole hearts were dissected and dissociated into single cells by treatment with TrypLE Express (Life Technologies) for 3 min at 37°C. Dissociated single cells were fixed and EdU detection was performed using the Click-iT Pacific Blue Flow Cytometry Assay Kit (Life Technologies). Cells were stained with 7-aminoactinomycin D (7-AAD; Life Technologies) for 30 min and analyzed on an LSR II flow cytometer (BD Biosciences). Data were analyzed using FlowJo software.

RNA isolation and quantitative PCR

Total RNA was isolated from embryonic hearts using the RNAqueous Micro Total RNA Isolation Kit (Ambion/Life Technologies). cDNA was generated using the High Capacity cDNA Reverse Transcriptase Kit (Applied Biosystems/Life Technologies) and qRT-PCR reactions were performed in triplicate using the Power SYBR Green Master Mix (Applied Biosystems) and run on a 7900HT Real-Time PCR system (Applied Biosystems). Relative abundance of mRNAs was calculated by normalization to *Actb* mRNA levels. Quantitative PCR data in all figures are presented as mean± s.d. Primer sequences are listed in Table S9.

RNA-Seq analysis

Whole-genome gene expression analysis was performed on RNA isolated from control and mutant embryonic hearts. Libraries were prepared using Illumina TruSeq Paired-End Cluster Kit v3, and sequenced with the Illumina HiSeq 2500 system for pair-ended 100 bp reads. Reads were aligned to the reference assembly NCBI37/mm9 (mouse) and assigned to genes using FeatureCounts (Liao et al., 2014). Differential expression was calculated using USeq (Nix et al., 2008). Differentially expressed genes were filtered with thresholds of FDR<0.05, clustered using Cluster 3.0 and visualized with Treeview (Eisen et al., 1998). GO analysis was conducted using DAVID (Huang et al., 2009). RNA-Seq datasets were analyzed and functional analyses were generated through the use of IPA (Qiagen, www.qiagen.com/ingenuity). GSEA was performed as described (Subramanian et al., 2005). RNA-Seq data have been deposited at GEO under accession numbers GSE74679 and GSE75151.

Calcium transients and electrophysiology

Cardiomyocytes isolated from E11.5 embryos were plated onto laminin-coated coverslips (#1, Warner Instruments). Briefly, beating myocytes were loaded with Fluo-4 (Thermo Fisher) for 20 min and then de-esterified for 20 min. Ca^{2+}-sensitive fluorescence signals were recorded using a filter set centered at 480 nm excitation and 535 nm emission (#49011, Chroma Technology), then low-pass filtered at 2 kHz and digitized at 5 kHz for 30 s per data file. Mean background emission was subtracted and changes in fluorescence amplitudes were expressed relative to the mean diastolic level attained between spontaneous beats (i.e. F/F_o). In a small number of additional experiments, Fluo-4-loaded cells were subjected to amphotericin B-perforated patch clamp (Spencer et al., 2014). Detailed methods are provided in the supplementary Materials and Methods.

Chromatin immunoprecipitation (ChIP)

Ninety E11.5 *Tnnt2::Cre;Kmt2d*$^{fl/fl}$ hearts and 90 *Tnnt2::Cre;Kmt2d*$^{fl/+}$ control hearts were crosslinked with 1% formaldehyde, quenched with

Development (2016) 143, 810-821 doi:10.1242/dev.132688

125 mM glycine, washed in PBS, resuspended in lysis buffer and sonicated using a Bioruptor Standard (Diagenode). ChIP of histone modifications (ChIP-Seq) was performed according to Alexander et al. (2015) with minor modifications. For each antibody (H3K4me1, H3K4me2 and H3K4me3; Table S8) 3 µg were added to three control samples and three mutant samples (three biological replicates per genotype per antibody).

For each ChIP-Exo replicate, 5×10^7 cardiac myocytes were derived from E14 mouse ESCs via directed differentiation as previously described (Wamstad et al., 2012). Samples were incubated with 2 mM disuccinimidyl glutarate for 45 min before the crosslinking step. ChIP-Exo was performed as previously described (Serandour et al., 2013; Alexander et al., 2015) using 8 µg anti-KMT2D antibody (Lee et al., 2013). DNA libraries were gel purified and sequenced on an Illumina HiSeq 4000 to generate 50 bp single-end reads with >100 million reads per sample. The ChIP-Seq and ChIP-Exo analysis pipeline is provided in the supplementary Materials and Methods. RNA-Seq data have been deposited at Gene Expression Omnibus (GEO) under accession number GSE74679. ChIP-Seq and ChIP-Exo data have been deposited at GEO under accession number GSE75151.

Statistical analyses

Data are reported as mean±s.d. and calculated using GraphPad Prism 6 software. Student's *t*-test (unpaired, two-tailed) was used when comparing mutant and control groups, with $P<0.05$ considered significant. Hypergeometric tests were performed to determine whether genes with decreased expression were more likely to be correlated with genes with decreased H3K4 methylation. The expressed gene set contained any gene with FPKM≥0.1 in either the control or *Tnnt2::Cre;Kmt2d*$^{fl/fl}$ mutants (21,664 genes).

Acknowledgements

We dedicate this work to the memory of Ian Spencer. We thank John Wylie for technical assistance; Dario Miguel-Perez for assistance with mouse husbandry; members of the B.G.B. lab for helpful discussions; C. Miller (Gladstone Histology Core) for histology; R. Chadwick and L. Ta (Gladstone Genomics Core) for RNA-Seq library preparation; A. Williams and S. Thomas (Gladstone Bioinformatics Core) for data analysis.

Competing interests

The authors declare no competing or financial interests.

Author contributions

S.-Y.A. designed and performed most of the experiments, analyzed data and wrote the manuscript. A.U. performed ChIP-Seq, ChIP-Exo and related analyses. C.I.S. performed calcium and electrophysiology studies. Y.H. performed echocardiography. J.-E.L. and K.G. generated the *Kmt2d*$^{fl/fl}$ mice and KMT2D antibody. B.G.B. designed experiments, directed the project and helped write the manuscript.

Funding

S.-Y.A. was supported by a graduate fellowship from Agency of Science, Technology and Research Singapore (A*STAR). Work in the K.G. laboratory was supported by the Intramural Research Program of the National Institutes of Health (NIH)/National Institute of Diabetes and Digestive and Kidney Diseases (NIDDK). B.G.B. was supported by a grant from NIH/National Heart, Lung, and Blood Institute (NHLBI) [NHLBI Bench to Bassinet Program, U01HL098179/UM1HL098179], by the Lawrence J. and Florence A. DeGeorge Charitable Trust/American Heart Association Established Investigator Award, an NIH/National Center for Research Resources (NCRR) grant [C06 RR018928] to the J. David Gladstone Institutes, and by William H. Younger, Jr. Deposited in PMC for immediate release.

Supplementary information

Supplementary information available online at
http://dev.biologists.org/lookup/suppl/doi:10.1242/dev.132688/-/DC1

References

Abela, D., Ritchie, H., Ababneh, D., Gavin, C., Nilsson, M. F., Khan, M. K., Carlsson, K. and Webster, W. S. (2010). The effect of drugs with ion channel-blocking activity on the early embryonic rat heart. *Birth Defects Res. B Dev. Reprod. Toxicol.* **89**, 429-440.

Alexander, J. M., Hota, S. K., He, D., Thomas, S., Ho, L., Pennacchio, L. A. and Bruneau, B. G. (2015). Brg1 modulates enhancer activation in mesoderm lineage commitment. *Development* **142**, 1418-1430.

Bayeva, M., Khechaduri, A., Wu, R., Burke, M. A., Wasserstrom, A., Singh, N., Liesa, M., Shirihai, O. S., Langer, N. B., Paw, B. H. et al. (2013). ATP-binding cassette B10 regulates early steps of heme synthesis. *Circ. Res.* **113**, 279-287.

Bernstein, B. E., Kamal, M., Lindblad-Toh, K., Bekiranov, S., Bailey, D. K., Huebert, D. J., McMahon, S., Karlsson, E. K., Kulbokas, E. J., Gingeras, T. R. et al. (2005). Genomic maps and comparative analysis of histone modifications in human and mouse. *Cell* **120**, 169-181.

Boudeau, J., Miranda-Saavedra, D., Barton, G. J. and Alessi, D. R. (2006). Emerging roles of pseudokinases. *Trends Cell Biol.* **16**, 443-452.

Chang, C.-P. and Bruneau, B. G. (2012). Epigenetics and cardiovascular development. *Annu. Rev. Physiol.* **74**, 41-68.

Cho, S.-J., Teng, I.-F., Zhang, M., Yin, T., Jung, Y.-S., Zhang, J. and Chen, X. (2015). Hypoxia-inducible factor 1 alpha is regulated by RBM38, a RNA-binding protein and a p53 family target, via mRNA translation. *Oncotarget* **6**, 305-316.

Creyghton, M. P., Cheng, A. W., Welstead, G. G., Kooistra, T., Carey, B. W., Steine, E. J., Hanna, J., Lodato, M. A., Frampton, G. M., Sharp, P. A. et al. (2010). Histone H3K27ac separates active from poised enhancers and predicts developmental state. *Proc. Natl. Acad. Sci. USA* **107**, 21931-21936.

Danielsson, B. R., Skold, A.-C. and Azarbayjani, F. (2001). Class III antiarrhythmics and phenytoin: teratogenicity due to embryonic cardiac dysrhythmia and reoxygenation damage. *Curr. Pharm. Des.* **7**, 787-802.

Danielsson, B. R., Danielsson, C. and Nilsson, M. F. (2007). Embryonic cardiac arrhythmia and generation of reactive oxygen species: common teratogenic mechanism for IKr blocking drugs. *Reprod. Toxicol.* **24**, 42-56.

Devine, W. P., Whythe, J. D., George, M., Koshiba-Takeuchi, K. and Bruneau, B. G. (2014). Early patterning and specification of cardiac progenitors in gastrulating mesoderm. *Elife* **3**, e03848.

Digilio, M. C., Marino, B., Toscano, A., Giannotti, A. and Dallapiccola, B. (2001). Congenital heart defects in Kabuki syndrome. *Am. J. Med. Genet.* **100**, 269-274.

Duranteau, J., Chandel, N. S., Kulisz, A., Shao, Z. and Schumacker, P. T. (1998). Intracellular signaling by reactive oxygen species during hypoxia in cardiomyocytes. *J. Biol. Chem.* **273**, 11619-11624.

Eisen, M. B., Spellman, P. T., Brown, P. O. and Botstein, D. (1998). Cluster analysis and display of genome-wide expression patterns. *Proc. Natl. Acad. Sci. USA* **95**, 14863-14868.

Forristal, C. E., Wright, K. L., Hanley, N. A., Oreffo, R. O. C. and Houghton, F. D. (2010). Hypoxia inducible factors regulate pluripotency and proliferation in human embryonic stem cells cultured at reduced oxygen tensions. *Reproduction* **139**, 85-97.

Guo, C., Chen, L. H., Huang, Y., Chang, C.-C., Wang, P., Pirozzi, C. J., Qin, X., Bao, X., Greer, P. K., McLendon, R. E. et al. (2013). KMT2D maintains neoplastic cell proliferation and global histone H3 lysine 4 monomethylation. *Oncotarget* **4**, 2144-2153.

He, A., Kong, S. W., Ma, Q. and Pu, W. T. (2011). Co-occupancy by multiple cardiac transcription factors identifies transcriptional enhancers active in heart. *Proc. Natl. Acad. Sci. USA* **108**, 5632-5637.

Hu, D., Gao, X., Morgan, M. A., Herz, H.-M., Smith, E. R. and Shilatifard, A. (2013). The MLL3/MLL4 branches of the COMPASS family function as major histone H3K4 monomethylases at enhancers. *Mol. Cell. Biol.* **33**, 4745-4754.

Huang, D. W., Sherman, B. T. and Lempicki, R. A. (2009). Systematic and integrative analysis of large gene lists using DAVID bioinformatics resources. *Nat. Protoc.* **4**, 44-57.

Infante, A., Laresgoiti, U., Fernández-Rueda, J., Fullaondo, A., Galán, J., Díaz-Uriarte, R., Malumbres, M., Field, S. J. and Zubiaga, A. M. (2008). E2F2 represses cell cycle regulators to maintain quiescence. *Cell Cycle* **7**, 3915-3927.

Iyer, N. V., Kotch, L. E., Agani, F., Leung, S. W., Laughner, E., Wenger, R. H., Gassmann, M., Gearhart, J. D., Lawler, A. M., Yu, A. Y. et al. (1998). Cellular and developmental control of O2 homeostasis by hypoxia-inducible factor 1 alpha. *Genes Dev.* **12**, 149-162.

Jiao, K., Kulessa, H., Tompkins, K., Zhou, Y., Batts, L., Baldwin, H. S. and Hogan, B. L. M. (2003). An essential role of Bmp4 in the atrioventricular septation of the mouse heart. *Genes Dev.* **17**, 2362-2367.

Kaikkonen, M. U., Spann, N. J., Heinz, S., Romanoski, C. E., Allison, K. A., Stender, J. D., Chun, H. B., Tough, D. F., Prinjha, R. K., Benner, C. et al. (2013). Remodeling of the enhancer landscape during macrophage activation is coupled to enhancer transcription. *Mol. Cell* **51**, 310-325.

Kisanuki, Y. Y., Hammer, R. E., Miyazaki, J., Williams, S. C., Richardson, J. A. and Yanagisawa, M. (2001). Tie2-Cre transgenic mice: a new model for endothelial cell-lineage analysis in vivo. *Dev. Biol.* **230**, 230-242.

Lauberth, S. M., Nakayama, T., Wu, X., Ferris, A. L., Tang, Z., Hughes, S. H. and Roeder, R. G. (2013). H3K4me3 interactions with TAF3 regulate preinitiation complex assembly and selective gene activation. *Cell* **152**, 1021-1036.

Lee, J.-E., Wang, C., Xu, S., Cho, Y.-W., Wang, L., Feng, X., Baldridge, A., Sartorelli, V., Zhuang, L., Peng, W. et al. (2013). H3K4 mono- and di-methyltransferase MLL4 is required for enhancer activation during cell differentiation. *Elife* **2**, e01503.

Lewandoski, M., Meyers, E. N. and Martin, G. R. (1997). Analysis of Fgf8 gene function in vertebrate development. *Cold Spring Harb. Symp. Quant. Biol.* **62**, 159-168.

Li, Q., Huang, Y., Spencer, C. I., Foley, A., Vedantham, V., Liu, L., Conway, S. J., Fu, J.-D. and Srivastava, D. (2012). *In vivo* reprogramming of murine cardiac fibroblasts into induced cardiomyocytes. *Nature* **485**, 593-598.
Liao, Y., Smyth, G. K. and Shi, W. (2014). FeatureCounts: an efficient general purpose program for assigning sequence reads to genomic features. *Bioinformatics* **30**, 923-930.
Lupien, M., Eeckhoute, J., Meyer, C. A., Wang, Q., Zhang, Y., Li, W., Carroll, J. S., Liu, X. S. and Brown, M. (2008). FoxA1 translates epigenetic signatures into enhancer-driven lineage-specific transcription. *Cell* **132**, 958-970.
Matsumoto, N. and Niikawa, N. (2003). Kabuki Make-up Syndrome: a review. *Am. J. Med. Genet. C Semin. Med. Genet.* **117C**, 57-65.
Miyamoto, S., Hidaka, K., Jin, D. and Morisaki, T. (2009). RNA-binding proteins Rbm38 and Rbm24 regulate myogenic differentiation via p21-dependent and -independent regulatory pathways. *Genes Cells* **14**, 1241-1252.
Moens, C. B., Stanton, B. R., Parada, L. F. and Rossant, J. (1993). Defects in heart and lung development in compound heterozygotes for two different targeted mutations at the N-myc locus. *Development* **119**, 485-499.
Muzumdar, M. D., Tasic, B., Miyamichi, K., Li, L. and Luo, L. (2007). A global double-fluorescent Cre reporter mouse. *Genesis* **45**, 593-605.
Ng, S. B., Bigham, A. W., Buckingham, K. J., Hannibal, M. C., McMillin, M. J., Gildersleeve, H. I., Beck, A. E., Tabor, H. K., Cooper, G. M., Mefford, H. C. et al. (2010). Exome sequencing identifies MLL2 mutations as a cause of Kabuki syndrome. *Nat. Genet.* **42**, 790-793.
Nix, D. A., Courdy, S. J. and Boucher, K. M. (2008). Empirical methods for controlling false positives and estimating confidence in ChIP-Seq peaks. *BMC Bioinformatics* **9**, 523.
Nord, A. S., Blow, M. J., Attanasio, C., Akiyama, J. A., Holt, A., Hosseini, R., Phouanenavong, S., Plajzer-Frick, I., Shoukry, M., Afzal, V. et al. (2013). Rapid and pervasive changes in genome-wide enhancer usage during mammalian development. *Cell* **155**, 1521-1531.
Ong, C.-T. and Corces, V. G. (2011). Enhancer function: new insights into the regulation of tissue-specific gene expression. *Nat. Rev. Genet.* **12**, 283-293.
Ortega-Molina, A., Boss, I. W., Canela, A., Pan, H., Jiang, Y., Zhao, C., Jiang, M., Hu, D., Agirre, X., Niesvizky, I. et al. (2015). The histone lysine methyltransferase KMT2D sustains a gene expression program that represses B cell lymphoma development. *Nat. Med.* **21**, 1199-1208.
Parlakian, A., Tuil, D., Hamard, G., Tavernier, G., Hentzen, D., Concordet, J.-P., Paulin, D., Li, Z. and Daegelen, D. (2004). Targeted inactivation of serum response factor in the developing heart results in myocardial defects and embryonic lethality. *Mol. Cell. Biol.* **24**, 5281-5289.
Pekowska, A., Benoukraf, T., Ferrier, P. and Spicuglia, S. (2010). A unique H3K4me2 profile marks tissue-specific gene regulation. *Genome Res.* **20**, 1493-1502.
Popova, E. Y., Xu, X., Dewan, A. T., Salzberg, A. C., Berg, A., Hoh, J., Zhang, S. S. and Barnstable, C. J. (2012). Stage and gene specific signatures defined by histones H3K4me2 and H3K27me3 accompany mammalian retina maturation in vivo. *PLoS ONE* **7**, e46867.
Ruthenburg, A. J., Allis, C. D. and Wysocka, J. (2007). Methylation of lysine 4 on histone H3: intricacy of writing and reading a single epigenetic mark. *Mol. Cell* **25**, 15-30.
Saga, Y., Miyagawa-Tomita, S., Takagi, A., Kitajima, S., Miyazaki, J. and Inoue, T. (1999). MesP1 is expressed in the heart precursors cells and required for the formation of a single heart tube. *Development* **126**, 3437-3447.
Serandour, A. A., Brown, G. D., Cohen, J. D. and Carroll, J. S. (2013). Development of an Illumina-based ChIP-exonuclease method provides insight into FoxA1-DNA binding properties. *Genome Biol.* **14**, R147.
Shah, M., Bogucki, B., Mavers, M., deMello, D. E. and Knutsen, A. (2005). Cardiac conduction abnormalities and congenital immunodeficiency in a child with Kabuki syndrome: case report. *BMC Med. Genet.* **6**, 28.
Shilatifard, A. (2012). The COMPASS family of histone H3K4 methylases: mechanisms of regulation in development and disease pathogenesis. *Annu. Rev. Biochem.* **81**, 65-95.
Sköld, A.-C., Wellfelt, K. and Danielsson, B. R. (2001). Stage-specific skeletal and visceral defects of the I Kr-blocker almokalant: further evidence for teratogenicity via a hypoxia-related mechanism. *Teratology* **64**, 292-300.
Spencer, C. I., Baba, S., Nakamura, K., Hua, E. A., Sears, M. A. F., Fu, C.-C., Zhang, J., Balijepalli, S., Tomoda, K., Hayashi, Y. et al. (2014). Calcium transients closely reflect prolonged action potentials in iPSC models of inherited cardiac arrhythmia. *Stem Cell Rep.* **3**, 269-281.
Stein, A. B., Jones, T. A., Herron, T. J., Patel, S. R., Day, S. M., Noujaim, S. F., Milstein, M. L., Klos, M., Furspan, P. B., Jalife, J. et al. (2011). Loss of H3K4 methylation destabilizes gene expression patterns and physiological functions in adult murine cardiomyocytes. *J. Clin. Invest.* **121**, 2641-2650.
Subramanian, A., Tamayo, P., Mootha, V. K., Mukherjee, S., Ebert, B. L., Gillette, M. A., Paulovich, A., Pomeroy, S. L., Golub, T. R., Lander, E. S. et al. (2005). Gene set enrichment analysis: a knowledge-based approach for interpreting genome-wide expression profiles. *Proc. Natl. Acad. Sci. USA* **102**, 15545-15550.
Thu, V. T., Kim, H. K., Ha, S. H., Yoo, J.-Y., Park, W. S., Kim, N., Oh, G. T. and Han, J. (2010). Glutathione peroxidase 1 protects mitochondria against hypoxia/reoxygenation damage in mouse hearts. *Pflugers Arch.* **460**, 55-68.
Ueda, K., Valdivia, C., Medeiros-Domingo, A., Tester, D. J., Vatta, M., Farrugia, G., Ackerman, M. J. and Makielski, J. C. (2008). Syntrophin mutation associated with long QT syndrome through activation of the nNOS-SCN5A macromolecular complex. *Proc. Natl. Acad. Sci. USA* **105**, 9355-9360.
van Loo, P. F., Mahtab, E. A. F., Wisse, L. J., Hou, J., Grosveld, F., Suske, G., Philipsen, S. and Gittenberger-de Groot, A. C. (2007). Transcription factor Sp3 knockout mice display serious cardiac malformations. *Mol. Cell. Biol.* **27**, 8571-8582.
Verzi, M. P., McCulley, D. J., De Val, S., Dodou, E. and Black, B. L. (2005). The right ventricle, outflow tract, and ventricular septum comprise a restricted expression domain within the secondary/anterior heart field. *Dev. Biol.* **287**, 134-145.
Wamstad, J. A., Alexander, J. M., Truty, R. M., Shrikumar, A., Li, F., Eilertson, K. E., Ding, H., Wylie, J. N., Pico, A. R., Capra, J. A. et al. (2012). Dynamic and coordinated epigenetic regulation of developmental transitions in the cardiac lineage. *Cell* **151**, 206-220.
Webster, W. S., Brown-Woodman, P. D. C., Snow, M. D. and Danielsson, B. R. G. (1996). Teratogenic potential of almokalant, dofetilide, and d-sotalol: drugs with potassium channel blocking activity. *Teratology* **53**, 168-175.
Wellfelt, K., Sköld, A.-C., Wallin, A. and Danielsson, B. R. (1999). Teratogenicity of the class III antiarrhythmic drug almokalant. Role of hypoxia and reactive oxygen species. *Reprod. Toxicol.* **13**, 93-101.
Yuan, S.-M. (2013). Congenital heart defects in Kabuki syndrome. *Cardiol. J.* **20**, 121-124.
Zaidi, S., Choi, M., Wakimoto, H., Ma, L., Jiang, J., Overton, J. D., Romano-Adesman, A., Bjornson, R. D., Breitbart, R. E., Brown, K. K. et al. (2013). De novo mutations in histone-modifying genes in congenital heart disease. *Nature* **498**, 220-223.
Zhang, X.-Q., Ahlers, B. A., Tucker, A. L., Song, J., Wang, J., Moorman, J. R., Mounsey, J. P., Carl, L. L., Rothblum, L. I. and Cheung, J. Y. (2006). Phospholemman inhibition of the cardiac Na+/Ca2+ exchanger: role of phosphorylation. *J. Biol. Chem.* **281**, 7784-7792.
Zhang, J., Parvin, J. and Huang, K. (2012). Redistribution of H3K4me2 on neural tissue specific genes during mouse brain development. *BMC Genomics* **13** Suppl. 8, S5.
Zhang, J., Dominguez-Sola, D., Hussein, S., Lee, J.-E., Holmes, A. B., Bansal, M., Vlasevska, S., Mo, T., Tang, H., Basso, K. et al. (2015). Disruption of *KMT2D* perturbs germinal center B cell development and promotes lymphomagenesis. *Nat. Med.* **21**, 1190-1198.

Supplementary Materials and Methods

(I) Supplementary Methods

Whole mount immunostaining

E12.5 embryonic hearts were dissected out and fixed in 4% paraformaldehyde for 3 hours, washed in PBT (PBS with 0.1% Tween), and incubated in blocking solution (5% serum, PBS, 0.5% Triton X-100) for 2 hours. Primary antibodies incubation was at 4˚C overnight in blocking solution. Hearts were washed with PBT and incubated with secondary antibodies at 4˚C overnight in blocking solution. Hearts were washed with PBT, fixed again in 4% paraformaldehyde for 2 hours, and then washed with PBT. Images were captured on Leica MZFLIII Microscope and antibodies used are listed in Table S8.

Calcium transients and electrophysiology

Cardiomyocytes isolated from E11.5 embryos were plated onto laminin-coated coverslips (#1, Warner Instruments). After visible beating was confirmed, the myocytes were loaded with the Ca^{2+}-sensitive fluorescent indicator Fluo-4. Each whole coverslip was exposed to the cell membrane-permeant Fluo-4 AM, using a 1:10 mixture of the indicator (dissolved in dry dimethyl sulfoxide at 5 mM) plus Powerload concentrate (Life Technologies). This mixture was diluted 100-fold into extracellular Tyrode's solution and substituted for culture medium in dishes containing coverslips (final indicator concentration, 5 μM). Cells were loaded with indicator for 20 min at room temperature and placed in fresh extracellular solution for a further 20 min to allow for de-esterification, before recordings were taken. To commence experiments, a coverslip of indicator-loaded myocytes was placed in a superfusion bath (RC26-GLP, Warner Instruments) on a Nikon TiS inverted microscope equipped with a microfluorometer (IonOptix). The bathing solutions were warmed to 30°C with a superfusion system and heated perfusion pencil (AutoMate Scientific). The myocytes were superfused at a constant flow (DN series syringes, Warner Instruments) with modified Tyrode's extracellular solution containing (mM): NaCl 137, NaHEPES 10, dextrose 10, KCl 5, $CaCl_2$ 2, and

$MgCl_2$ 1, set to pH 7.4 with NaOH. Single, spontaneously contracting myocytes and small clusters (5 or fewer cells) were selected for study.

Fluo-4 fluorescence transients were recorded with a standard filter set with excitation centered on 480 nm and emission centered on 535 nm (#49011, Chroma Technology, Bellows Falls, VT). Fluorescence was obtained from contracting cells plus a cell-free border using a cell-framing adaptor (IonOptix). Between sampling periods, the excitation light was blocked with a shutter (Vincent Associates). Ca^{2+}-sensitive fluorescence signals were low-pass filtered at 2 kHz and digitized at 5 kHz for 30 s per data file. Mean durations for $[Ca^{2+}]_i$ transients were calculated by measuring up-to 40 individual responses per data file (depending on the spontaneous beating rate), corresponding to the sampling of one cell or cluster representing the particular genotype. Multiple samples were combined to get an overall mean to be used for graph plotting. Fluorescence signals were corrected by subtracting the mean background emission (present after removing the cell(s) from the field of view) from all data files, and changes in fluorescence amplitudes were expressed relative to the mean diastolic level attained between spontaneous beats (i.e. F/F_o). Changes in this relative fluorescence were considered to reflect underlying changes in intracellular Ca^{2+} concentration. In a small number of additional experiments, Fluo-4 loaded cells were subjected to amphotericin B-perforated patch clamp (Spencer et al., 2014). Briefly, patch electrodes of approximately 2-4 MΩ (WPI) were tip-filled by dipping (for 20 s) in an intracellular solution containing (mM): KCl 120, NaHEPES 20, MgATP 10, K_2EGTA 5, $MgCl_2$ 2, adjusted to pH 7.1 with KOH, and then back filled with the same solution including amphotericin B (240 µg/ml). The action potentials associated with spontaneous $[Ca^{2+}]_i$ transients, were recorded (at 5 kHz as above) in current clamp mode with zero applied current, and were corrected for a –5.6 mV liquid junction potential. Unless stated otherwise, all reagents were from Sigma-Aldrich.

Chromatin immunoprecipitation (ChIP)

90 *Tnnt2::Cre;Kmt2d*$^{fl/fl}$ hearts and 90 *Tnnt2::Cre;Kmt2d*$^{fl/+}$ control hearts (from littermates) were collected at embryonic day 11.5. Formaldehyde was added to a final concentration of 1% to generate DNA-protein crosslinks for 10 minutes at room temperature, then quenched by adding glycine to a final concentration of 125mM. Hearts were pelleted at 430g at 4C for 5 minutes and washed twice in 10mL of ice-cold PBS. Hearts were then resuspended in 3mL of ice-cold cell lysis buffer (5mM PIPES, pH 8.0; 85mM KCl; 1.0% (v/v) NP- 40; 1x protease inhibitor cocktail) and incubated on ice for 15 minutes. Next, hearts were homogenized on ice using 20 strokes on a Dounce tissue grinder (Sigma-Aldrich). Homogenate was pelleted at 430g at 4C for 5 minutes, then resuspended in ice-cold nuclei lysis buffer (50mM Tris-Cl, pH 8.0; 10mM EDTA, pH 8.0; 1% (w/v) SDS; 1x protease inhibitor cocktail). Samples were incubated in nuclei lysis buffer for 30 minutes on ice and sonicated using a Bioruptor Standard (Diagenode) (6x5min cycles, 30s on/30s off, 4C) to shear chromatin into 200- 600bp fragments. Samples were pelleted for 10 minutes at 20,800xg at 4C and supernatants were diluted 1:5 with IP dilution buffer (50mM Tris-Cl, pH 7.4; 150mM NaCl, 1mM EDTA, pH 8.0; 1% (v/v) NP-40; 0.25% (w/v) sodium deoxycholate; 1x protease inhibitor cocktail). 3 ug of anti-H3K4me1 antibody, 3 ug of anti-H3K4me2 antibody, or 3 ug of anti-H3K4me3 antibody (listed in Table S8) were added to 3 control samples and 3 mutant samples (3 biological replicates per genotype per antibody). Samples were incubated overnight at 4˚C.

40uL of Protein G Dynabead (Life Technologies) suspension was added to each sample, incubated for 2 hours, then washed twice with IP wash buffer 1 (IP dilution buffer without protease inhibitors), twice with IP wash buffer 2 (100mM Tris-Cl, pH 9.0; 500mM LiCl; 1% (v/v) NP-40; 1% (w/v) sodium deoxycholate), and with IP wash buffer 3 (100mM Tris-Cl, pH 9.0; 500mM LiCl; 150mM NaCl; 1% (v/v) NP-40; 1% (w/v) sodium deoxycholate). Immunoprecipitated material was eluted by incubating at 65C for 30 minutes with shaking in 100uL of ChIP elution buffer (50mM NaHCO3, 1% (w/v) SDS). NaCl was added to each eluted

sample to a final concentration of 0.54M, and crosslinks were reversed by overnight incubation at 67˚C. Samples were treated with 10ug of RNase A for 30 minutes at 37˚C, and DNA was precipitated from each sample by adding 1.8x the sample volume of AMPure XP magnetic bead suspension (Beckman Coulter). Beads were washed 2x with 80% ethanol, dried, and beads were resuspended in 20uL water to elute DNA. Prepared libraries (Kapa Biosystems) were sequenced in 1x50bp mode on Illumina HiSeq 2500.

ChIP-Exo

For each replicate, $5x10^7$ cardiac myocytes were derived from E14 mouse embryonic stem cells via directed differentiation as previously described (Wamstad et al., 2012). Cells were pelleted, washed and resuspended in PBS. Disuccinimidyl glutarate (DSG), a long-range crosslinking agent, was added to a final concentration of 2mM and incubated for 45 minutes. Cells were pelleted, washed and resuspended in PBS containing 1% (v/v) formaldehyde for 15 minutes at room temperature. Formaldehyde crosslinking was quenched by adding glycine to a final concentration of 125mM and incubating for 10 minutes. Cells were then washed 3 times with ice-cold PBS, pelleted and flash frozen. To complete ChIP-exo, frozen cells were thawed on ice; lysis, homogenization, sonication, and immunoprecipitation were performed in the same fashion as they were for ChIP-Seq. We used an anti-KMT2D antibody provided by Kai Ge (NIH) with 8 ug per replicate (Lee et al., 2013). Following immunoprecipitation, ChIP-exo was performed as previously described (Serandour et al., 2013). Briefly, prior to the elution of immunoprecipitated DNA-containing complexes from the Protein G beads, DNA was polished and ligated with the Illumina P7 adapter. Nicks were then repaired, followed by exonuclease digestion. Following digestion, immunoprecipitated complexes were eluted from the beads and crosslinks were reversed. DNA was isolated from the eluate and denatured. Double-stranded DNA was generated from each single strand using a primer which anneals to the P7 adapter sequence. The resulting fragments were ligated with P5 adapter, followed by amplification via PCR with indexed primers. The

resulting DNA libraries were gel-purified and sequenced on an Illumina HiSeq 4000 to generate 50bp single-end reads with >100 million reads per sample.

ChIP-Seq and ChIP-Exo analysis

Sequencing reads were de-multiplexed using CASAVA version 1.8.2. Reads are trimmed using the Fastq-mcf program (http://code.google.com/p/ea-utils). Filtered reads are analyzed using the Fastqc program (Babraham Bioinformatics, Cambridge, United Kingdom). Reads were then aligned to the mm9 genome assembly using bowtie2 (Langmead and Salzberg, 2012) and filtered to retain only reads with a mapq score greater than or equal to 30 using SAMtools version 1.2 (Li et al., 2009). For tag calling, bam2bed is used to convert bam files into bed files, and the genome-wide shift between + and – strand tags is calculated in a manner adapted from the Kundaje method (Neph et al., 2012). The mm9 genome assembly was then split into 20bp bins, and tag density is defined as the number of tags that map to within 75 bp of each genomic bin (Landt et al., 2012). For ChIP-Seq, the same calculation was performed for each sample's associated input, and tag densities were normalized to input as follows:
tagDensity = #binsInGenome * ((#tags/#totalTags) - (#inputTags/#totalInputTags))

Publicly available Illumina sequencing data from H3K4me1 and H3K4me3 ChIP-seq experiments using both mouse embryonic stem cells and cardiac myocytes generated via directed differentiation (Wamstad et al., 2012) was filtered and aligned to the mm9 genome assembly in an identical manner to that described for the H3K4me1 and H3K4me3 ChIP-seq experiments we performed using E11.5 hearts. The Spearman correlation between the aligned reads from each experiment was then determined using bamCorrelate, part of the deepTools package (Ramírez et al., 2014). This tool allows for the comparison of ChIP-Seq experiments prior to any further manipulation of the data, such as read density smoothing or peak calling.

For ChIP-Exo, no input chromatin was provided and the tag densities are normalized as follows (Landt et al., 2012):
tagDensityOfGenomicBin = #tagsAtBin * #binsInEntireGenome / #totalTagsInDataset
To minimize false positives and false negatives, bins representing greater than 4.9-fold enrichment over input (tag density score ≥ 30) are accepted for ChIP-Seq and and bins representing greater than 6.6-fold enrichment over background (tag density score ≥ 100) are accepted for ChIP-Exo. Enriched bins are merged together throughout the genome and merged bins representing signal peaks spanning multiple genomic bins are retained. For ChIP-Seq, a total of 358,833 peaks were identified. To compare peak scores and perform differential enrichment, peaks are annotated with total tag density within peak regions. For ChIP-Exo, KMT2D binding events were defined by peaks present in 2 out of 3 replicates within 500 bp of each other. Genomic regions were associated with genes using GREAT (Mclean et al., 2010), with gene regulatory domain defined as proximal for 5 kb upstream and 1 kb upstream, distal for up to 100 kb in both directions to the nearest gene's basal domain.

(II) Supplementary Figures

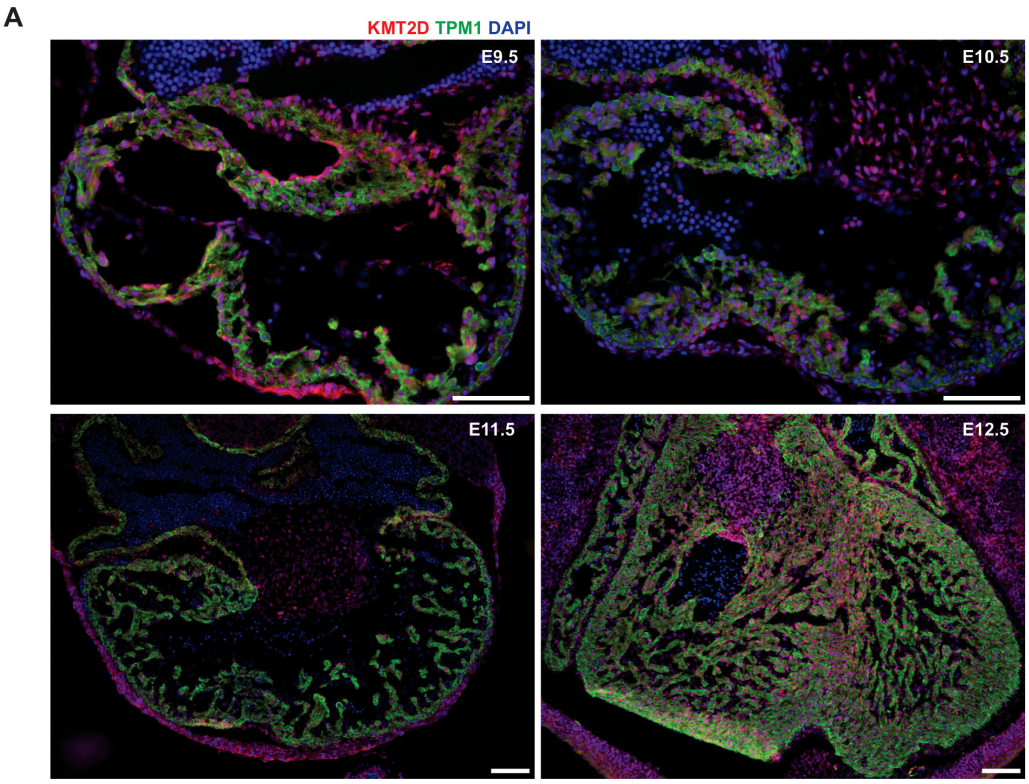

Fig. S1. KMT2D is expressed broadly in the developing heart.

(A) Immunostaining of E9.5, E10.5, E11.5 and E12.5 embryonic hearts in four-chamber view sections show ubiquitous KMT2D expression (green). Nuclei (DAPI) is stained in blue and the myocardium (TPM1) is stained in red. Scale bar = 100 μm.

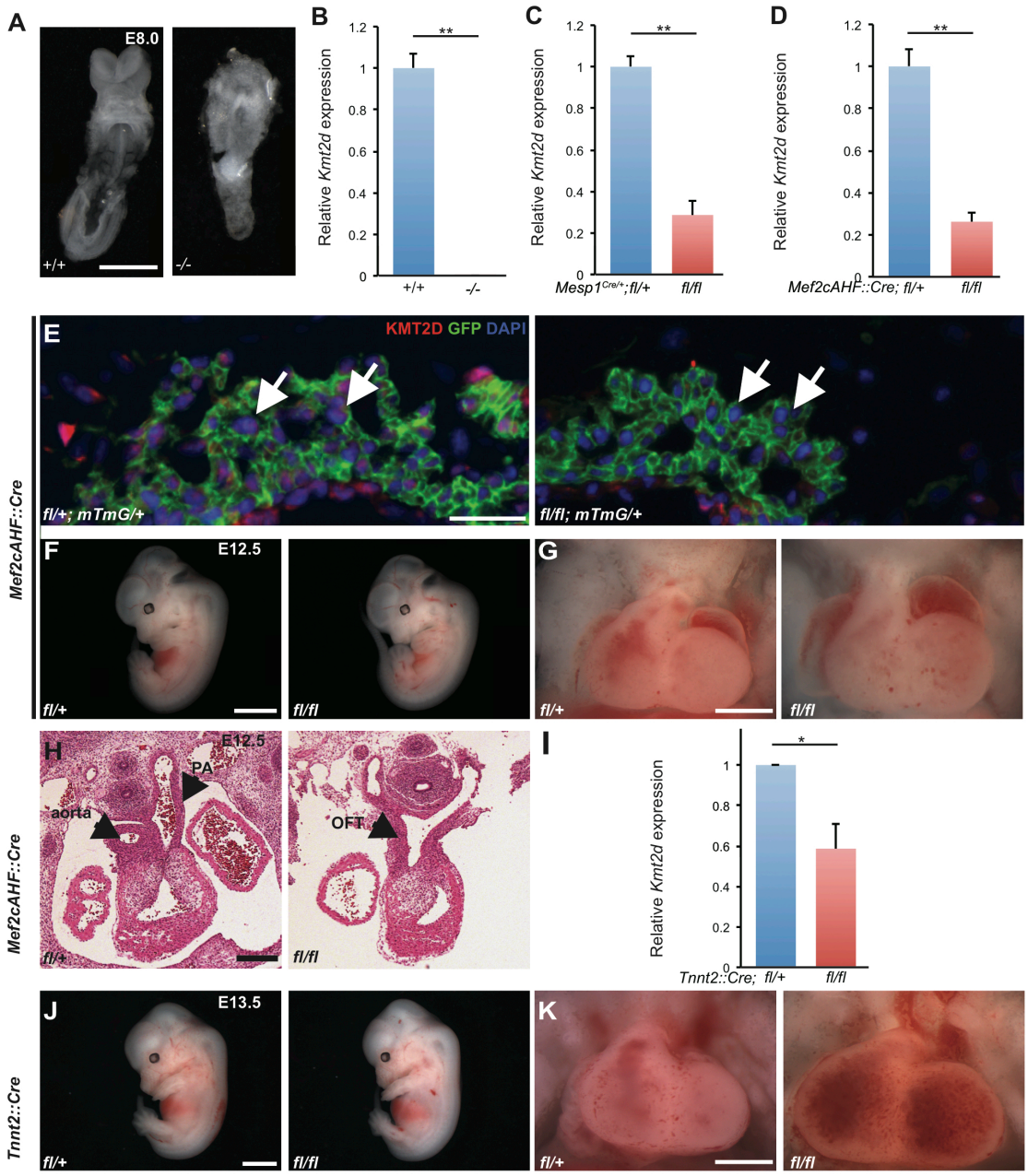

Fig. S2. Deletion of *Kmt2d* in cardiac precursors and myocardium leads to loss of *Kmt2d* expression and minor changes in gross morphology.

(A) Representative images of E8.0 control $Kmt2d^{+/+}$ and $Kmt2d^{\Delta/\Delta}$ embryos show severe developmental defects in mutants. Scale bar = 250 μm.

(B) qRT-PCR in E8.0 control $Kmt2d^{+/+}$ and $Kmt2d^{\Delta/\Delta}$ embryos show complete loss of *Kmt2d* transcript in mutants (P<0.01).

(C) qRT-PCR in E9.0 control *Mesp1*^{Cre};*Kmt2d*$^{fl/+}$ and *Mesp1*^{Cre};*Kmt2d*$^{fl/fl}$ whole hearts show 71.4% decrease in *Kmt2d* transcript levels in mutants (P<0.01).
(D) qRT-PCR in E11.5 control *Mef2cAHF::Cre;Kmt2d*$^{fl/+}$ and *Mef2cAHF::Cre;Kmt2d*$^{fl/fl}$ right ventricles and outflow tracts shows 73.8% decrease in *Kmt2d* transcript levels in mutants (P<0.01).
(E) E12.5 control and *Mef2cAHF::Cre;Kmt2d*$^{fl/fl}$ *Rosa*$^{mTmG/+}$ cardiac sections at four-chamber view are stained for KMT2D (red), GFP (green), DAPI (blue). Mutant interventricular septum shows loss of KMT2D expression in Cre-expressing GFP-positive cells. Scale bar = 100 μm.
(F) Representative images of E12.5 control and *Mef2cAHF::Cre;Kmt2d*$^{fl/fl}$ embryos show no obvious differences. Scale bar = 2 mm.
(G) Representative images of E12.5 control and *Mef2cAHF::Cre;Kmt2d*$^{fl/fl}$ hearts show no obvious differences. Scale bar = 500 μm.
(H) Representative images of E12.5 control and *Mef2cAHF::Cre;Kmt2d*$^{fl/fl}$ cardiac sections at four-chamber view show defects in outflow tract septation into pulmonary and aorta (arrows). Scale bar = 250 μm.
(I) qRT-PCR in E11.5 control and *Tnnt2::Cre;Kmt2d*$^{fl/fl}$ whole hearts shows 41.1% decrease in *Kmt2d* transcript levels (P<0.05). Incomplete loss is likely due to contribution of *Tnnt2::Cre*-negative non-myocyte population in hearts, including endocardium and cardiac fibroblasts.
(J) Representative images of E13.5 control and *Tnnt2::Cre;Kmt2d*$^{fl/fl}$ embryos show no obvious differences. Scale bar = 2 mm.
(K) Representative images of E13.5 control and *Tnnt2::Cre;Kmt2d*$^{fl/fl}$ hearts show no obvious differences. Scale bar = 250 μm.
PA, pulmonary artery; OFT, outflow tract. *P<0.05; **P< 0.01; error bars indicate SD.

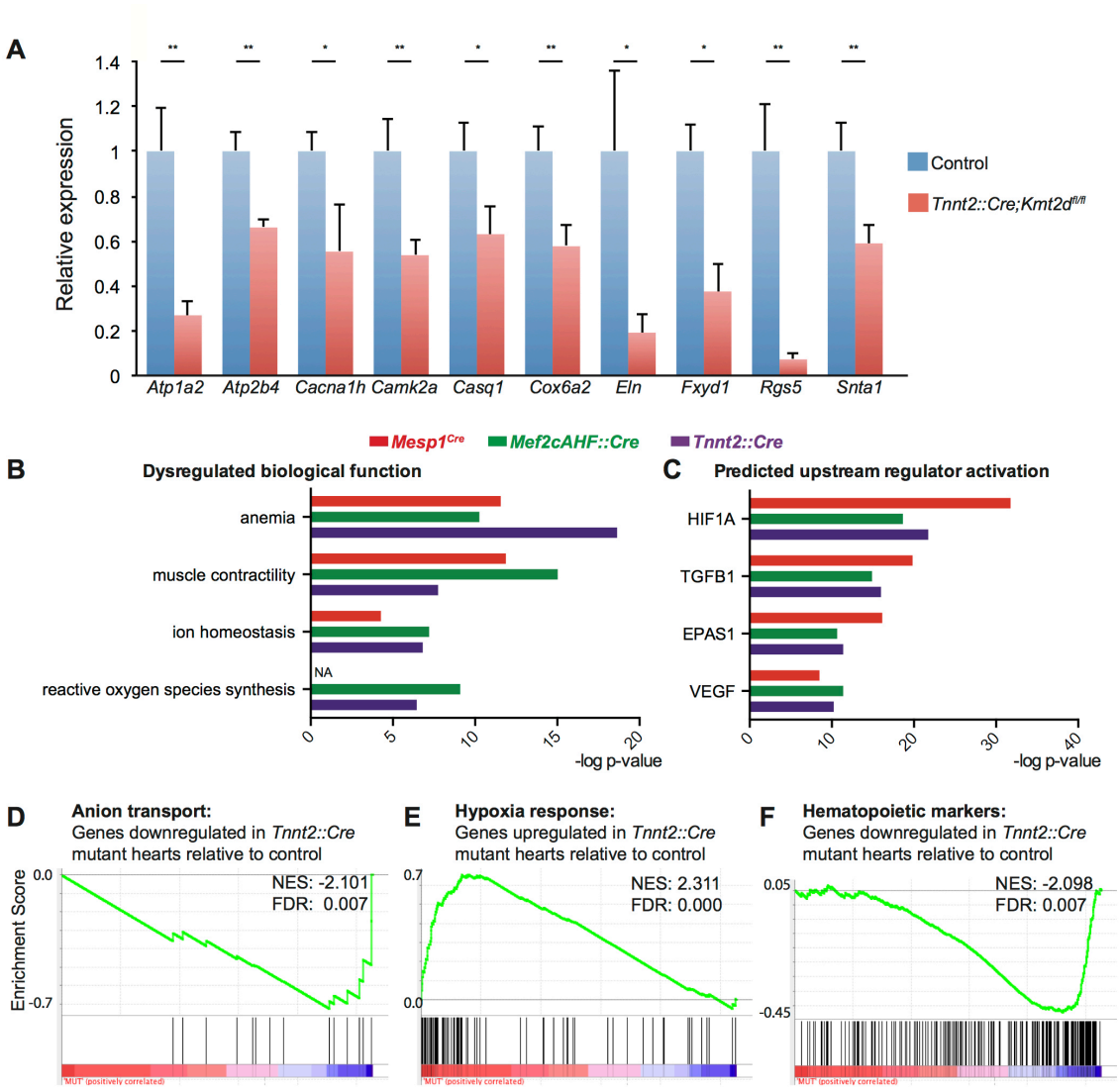

Fig. S3. Deletion of *Kmt2d* in cardiac precursors and myocardium lead to downregulation of ion transport genes and upregulation of hypoxia response genes.

(A) qRT-PCR in E11.5 control and *Tnnt2::Cre; Kmt2d*$^{fl/fl}$ embryos shows decreases in ion transport related genes (**P*< 0.05; ***P*< 0.01, error bars indicate SD).

(B) Ingenuity Pathway Analysis of differentially expressed genes in all three deletion genotypes shows that biological functions that were significantly dysregulated are associated with anemia, contractility of muscle, ion homeostasis and reactive oxygen species synthesis (*P*< 0.05).

(C) Ingenuity Pathway Analysis of differentially expressed genes in all three deletion genotypes shows that upstream regulators that were significantly predicted to be dysregulated are associated with hypoxia (P<0.05).
(D) GSEA shows a significant depletion of genes associated with anion transport in E11.5 *Tnnt2::Cre;Kmt2d*$^{fl/fl}$ mutants (FDR<0.01).
(E) GSEA shows a significant enrichment of genes associated with hypoxia response in E11.5 *Tnnt2::Cre;Kmt2d*$^{fl/fl}$ mutants (FDR<0.01).
(F) GSEA shows a significant depletion of genes associated with erythropoietic differentation in E11.5 *Tnnt2::Cre;Kmt2d*$^{fl/fl}$ mutants (FDR<0.01).

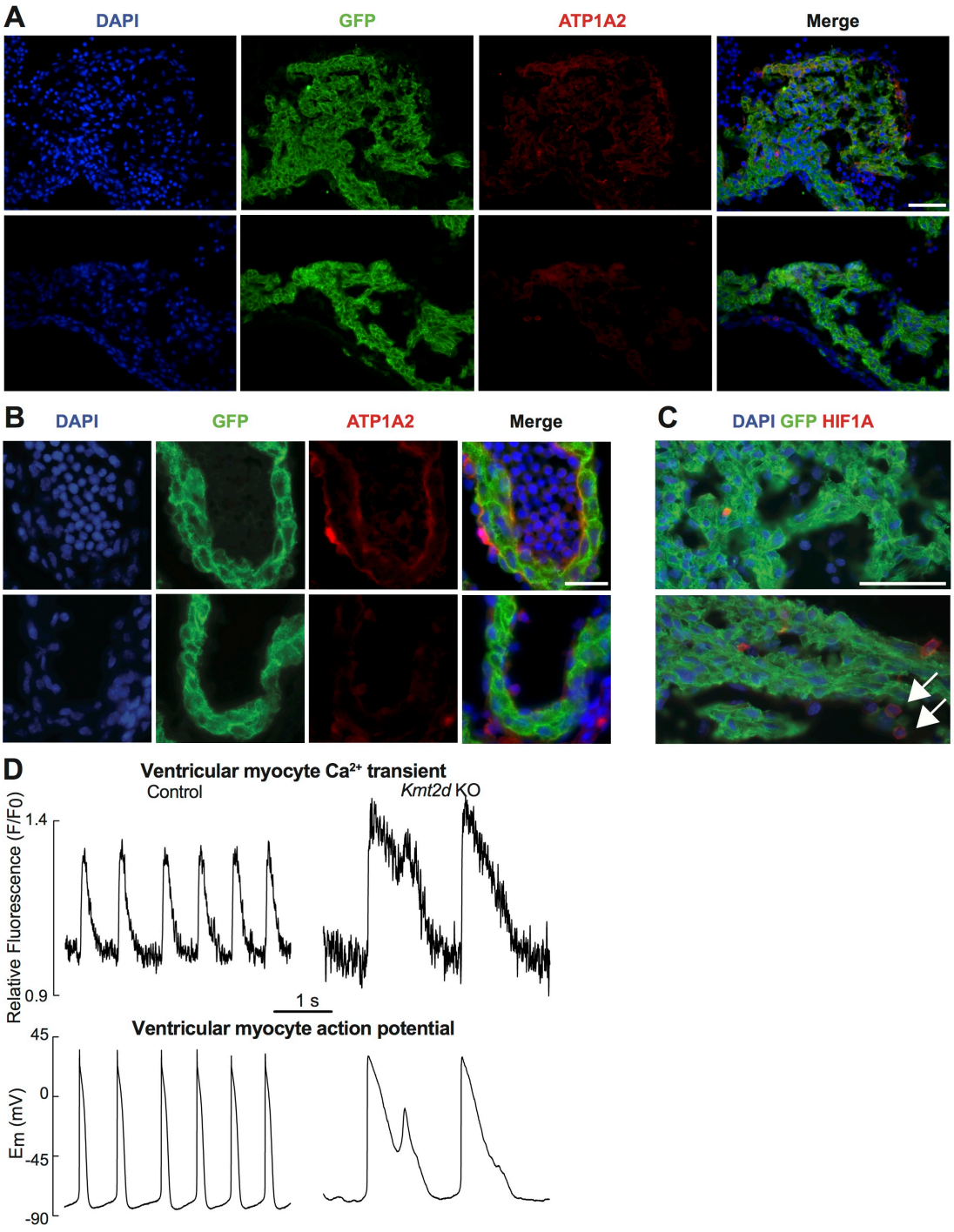

Fig. S4. Deletion of *Kmt2d* in myocardium leads to decreased expression of ion transporter ATP1A2, increased expression of hypoxia response factor HIF1A and altered calcium handling in ventricular myocytes.

(A) E11.5 control and *Tnnt2::Cre;Kmt2d*$^{fl/fl}$*; Rosa*$^{mTmG/+}$ cardiac sections at four-chamber view are stained for ATP1A2 (red), GFP (green) and DAPI (blue). Magnified image of interventricular septum shows loss of ATP1A2 expression in Cre-expressing GFP-positive cells. Scale bar = 50 μm.

(B) E11.5 control and *Tnnt2::Cre;Kmt2d*$^{fl/fl}$*; Rosa*$^{mTmG/+}$ cardiac sections at four-chamber view are stained for ATP1A2 (red), GFP (green) and DAPI (blue). Magnified image of left atria shows loss of ATP1A2 expression in Cre-expressing GFP-positive cells. Scale bar = 25 μm.

(C) E11.5 control and *Tnnt2::Cre;Kmt2d*$^{fl/fl}$*; Rosa*$^{mTmG/+}$ cardiac sections at four-chamber view are stained for HIF1A (red), GFP (green) and DAPI (blue). Magnified image of interventricular septum shows increase in HIF1A expression in GFP-negative cells (arrows). Scale bar = 50 μm.

(D) Fluo-4 fluorescence recordings (upper panel) and traces of action potentials (lower panel, E_m: membrane potential) from control and Tnnt2::Cre;*Kmt2d*$^{fl/fl}$ (*Kmt2d* KO) ventricular myocytes isolated at E11.5. Note the reduced action potential frequency, prolongation and secondary depolarization exhibited by the mutant cell, indicative of electrophysiological abnormality. Early after depolarizations (EADs) are observed in 3% of controls and 13% of *Kmt2d* KO ventricular myocytes.

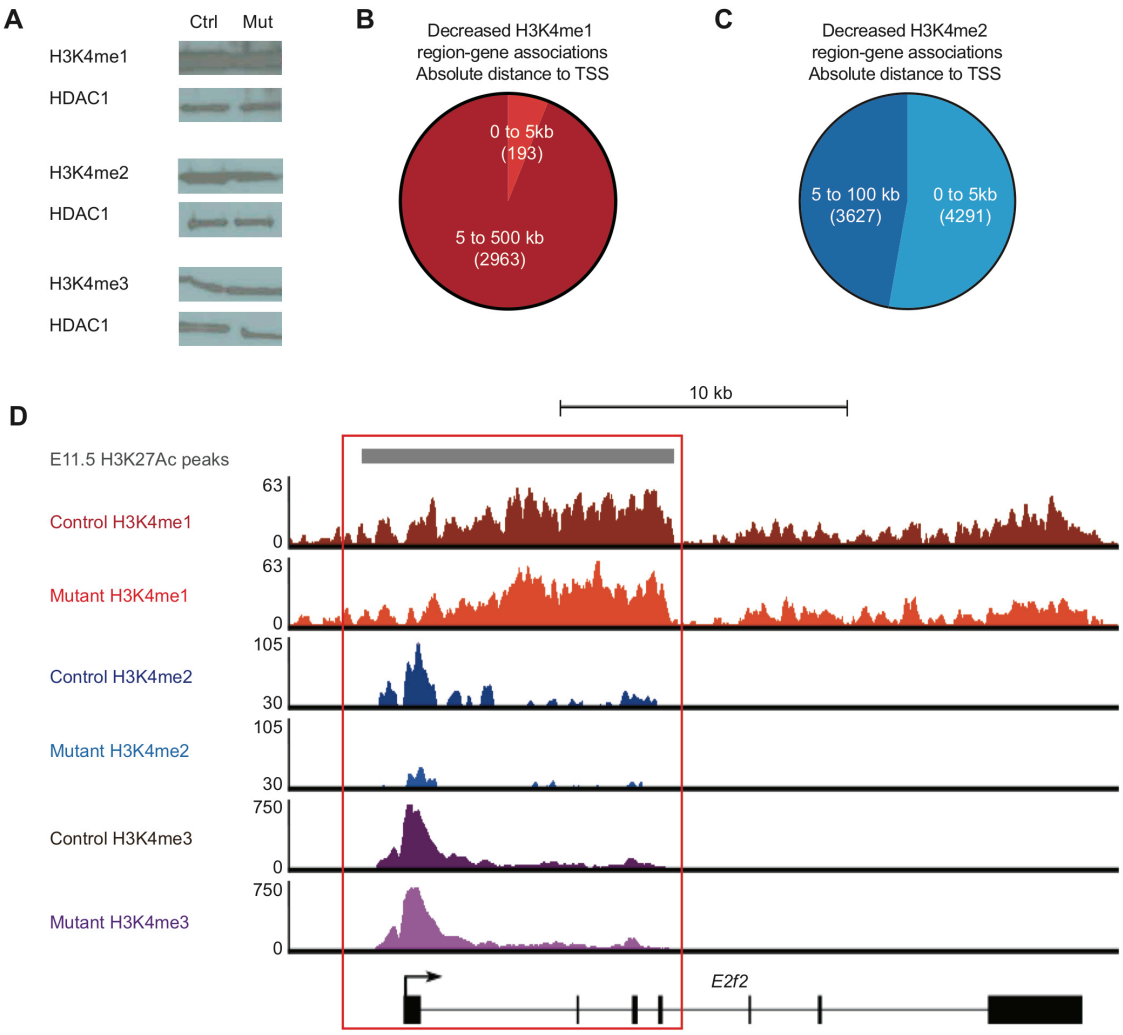

Fig. S5. Myocardial deletion of *Kmt2d* results in a decrease in H3K4me1 levels at regions distinct from that with decreased H3K4me2 levels.

(A) Western blot of H3K4me1, H3K4me2 and H3K4me3 bulk levels in E11.5 control *Tnnt2::Cre;Kmt2d*$^{fl/+}$ and *Tnnt2::Cre;Kmt2d*$^{fl/fl}$ hearts do not show obvious differences. HDAC1 is loading control.

(B) 2730 regions with decreased H3K4me1 levels (FDR<0.1) are assigned to 2473 genes by proximity within 100kb using Stanford GREAT. Decreased H3K4me1 region-gene associations are evaluated for absolute distance to TSS, showing that 193 region-gene associations are within 5 kb of TSS and 2963 region-gene associations are between 5 to 100 kb of TSS.

(C) 6417 regions with decreased H3K4me2 levels (FDR<0.1) are assigned to 6573 genes by proximity using Stanford GREAT. 3627 region-gene associations are within 5 kb of TSS and 4291 region-gene associations are between 5 to 100 kb of TSS.

(C) Venn diagram shows only 78 genes overlap between 2473 genes with decreased H3K4me1 levels and 492 genes downregulated in E11.5 *Tnnt2::Cre;Kmt2d*$^{fl/fl}$ hearts. GO categories of the subset of 78 genes are over-represented for ion transport and transcription regulation.

(D) Venn diagram representing overlap of 2730 regions with decreased H3K4me1 with 6699 regions with decreased H3K4me2. Of the overlapping 172 regions mapped to 186 genes, only 7 genes are downregulated in E11.5 *Tnnt2::Cre;Kmt2d*$^{fl/fl}$ hearts.

(E) Browser tracks showing average H3K4me1, H3K4me2 and H3K4me3 input normalized tag density at TSS of *E2f2*. Red box indicates region with decreased H3K4me2.

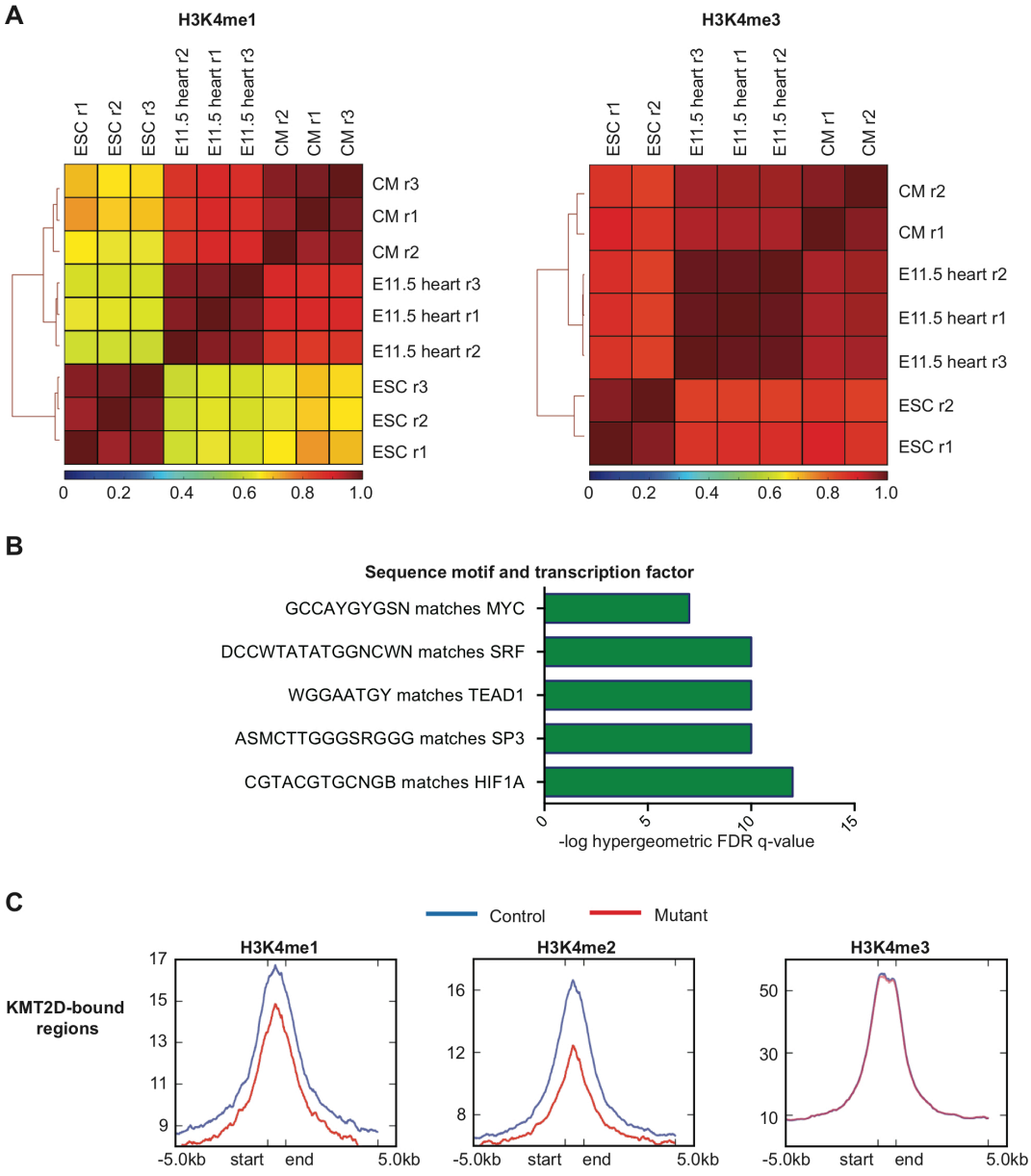

Fig. S6. KMT2D binds to promoter and enhancer regions with motifs matching transcription factors important for heart development.

(A) Spearman correlation of H3K4me1 and H3K4me3 ChIP-Seq data between embryonic stem cells (ESCs), derived cardiomyocytes (CM) (Wamstad et al., 2012) and E11.5 hearts show stronger correlation (red) of H3K4 methylation patterns between CM and E11.5 hearts, which are distinct from ESCs. r

represents replicate number and scale bar indicates Spearman correlation coefficient.

(B) Over-represented motifs found in KMT2D-bound regions match transcription factors important for heart development.

(C) Metagene profiles showing average distribution of H3K4me1, H3K4me2 and H3K4me3 input normalized tag density at KMT2D-bound regions sites in E11.5 control and *Tnnt2::Cre;Kmt2d*$^{fl/fl}$ hearts. Blue line denotes control hearts and red line denotes mutant hearts. Mutants show decreased H3K4me1 and H3K4me2 levels at KMT2D-bound regions, and no difference in H3K4me3 levels.

(III) Supplementary Tables

Table S1. Genotypes of offspring obtained from *Kmt2d* deletion by crossing *ACTB::Cre; Kmt2d*$^{\Delta/+}$ males with *ACTB::Cre; Kmt2d*$^{\Delta/+}$ females.

Deletion in tissue	Stage	Total animals	Heterozygotes	% heterozygotes	Null mutants	% null mutants
Global (*ACTB::Cre*)	E8.0	31	13	42	8	26
	E8.5	9	5	56	0	0
	E9.5	26	16	61	0	0
	P0	21	9	43	0	0
	P35	36	18	50	0	0

An additional 36 heterozygotes (*ACTB::Cre; Kmt2d*$^{\Delta/+}$) genotyped at P56 were obtained from crossing *ACTB::Cre* males with *Kmt2d*$^{fl/fl}$ females.

Table S2. Genotypes of offspring obtained from conditional *Kmt2d* deletion using *Mesp1*^{Cre}, *Mef2cAHF::Cre, Tnnt2::Cre* or *Tie2::Cre*.

Deletion in tissue	Stage	Total animals	Mutants	% mutants
Mesodermal precursors (*Mesp1*^{Cre})	E8.5	12	2	17
	E9.0	17	4	24
	E9.5	38	7	18
	E10.5	15	0	0
	E11.5	8	0	0
	E12.5	5	0	0
	P0	45	0	0
Anterior heart field precursors (*Mef2cAHF::Cre*)	E9.5	14	4	29
	E10.5	96	21	22
	E11.5	40	8	20
	E12.5	39	7	18
	E13.5	14	0	0
	P0	96	0	0
Myocardial cells (*Tnnt2::Cre*)	E10.5	55	17	31
	E11.5	414	104	25
	E12.5	31	8	26
	E13.5	19	5	26
	E14.5	18	0	0
	E16.5	6	0	0
	P0	55	0	0

Table S3.

Click here to Download Table S3

Table S4. Region-gene association distribution of H3K4me1 and H3K4me2 peaks.

Region-gene association	0 to 5 kb	% of peaks in 0 to 5 kb	50 to >500 kb	% of peaks in 50 to >500 kb
H3K4me1	35380	11.08%	284003	88.92%
H3K4me2	34144	11.28%	268429	88.72%

Table S5. Hypergeometric probability of downregulated genes with decreased H3K4 methylation associated with ion transport, compared to the population success of all downregulated genes associated with ion transport.

		H3K4me1	H3K4me2
Population size (P)	All downregulated genes	492	492
Number of successes in population (p)	Downregulated genes associated with ion transport	37	37
Ratio (p/P) in %	Ratio of (Downregulated genes associated with ion transport / All downregulated genes) in %	7.52%	7.52%
Sample size (S)	All downregulated genes with decreased H3K4 methylation	78	160
Number of successes in sample (s)	Downregulated genes with decreased H3K4 methylation associated with ion transport	8	18
Ratio (s/S) in %	Ratio of (Downregulated genes with decreased H3K4 methylation associated with ion transport / All downregulated genes with decreased H3K4 methylation) in %	10.25%	11.25%
Probability of drawing (number of s successes or more) in a sample of S, given (number of p successes) in population P	Hypergeometric probability	0.22	0.025

Table S6. Hypergeometric probability of downregulated genes with decreased H3K4 methylation compared to the population success of all expressed genes with decreased H3K4 methylation.

		H3K4me1	H3K4me2
Population size (P)	All expressed genes	21664	21664
Number of successes in population (p)	Expressed genes with decreased H3K4 methylation	2778	6315
Ratio (p/P) in %	Ratio of (Expressed genes with decreased H3K4 methylation/ All expressed genes) in %	12.80%	29.15%
Sample size (S)	All downregulated genes	492	492
Number of successes in sample (s)	Downregulated genes with decreased H3K4 methylation	78	160
Ratio (s/S) in %	Ratio of (Downregulated genes with decreased H3K4 methylation/ All downregulated genes) in %	15.80%	32.52%
Probability of drawing (number of s successes or more) in a sample of S, given (number of p successes) in population P	Hypergeometric probability	0.027	0.054

Table S7.

Click here to Download Table S7

Table S8. List of antibodies used in this study.

Antibody	**Company**	**Catalog No.**	**Host Isotype**	**Clone**	**Conjugate**
Anti-KMT2D	Sigma-Aldrich	HPA035977	Rabbit IgG	N.A.	N.A.
Anti-KMT2D	Kai Ge lab (Lee et al., 2013)	N.A.	Rabbit IgG	N.A.	N.A.
Anti-ATP1A2	Abcam	ab2871	Mouse IgG1	M7-PB-E9	N.A.
Anti-HIF1A	Abcam	ab1	Mouse IgG2b	H1alpha67	N.A.
Anti-GFP	Abcam	ab13970	Chicken IgY	N.A.	N.A.
Anti-TPM1	DSHB	N.A.	Mouse IgG1	CH-1	N.A.

Anti-PECAM-1	BD Pharmingen	55370	Rat IgG2a	N.A.	N.A.
Anti-HDAC1	Abcam	ab7028	Rabbit IgG	N.A.	N.A.
Anti-H3K4me1	Diagenode	C15410194	Rabbit IgG	pAb-194-050	N.A.
Anti-H3K4me2	Abcam	ab32356	Rabbit IgG	Y47	N.A.
Anti-H3K4me3	Millipore	07-473	Rabbit IgG	N.A.	N.A.
Anti-Rabbit Secondary	Invitrogen	A-11037	Goat	N.A.	Alexa 594
Anti-Mouse Secondary	Invitrogen	A-11032	Goat	N.A.	Alexa 594
Anti-Rat Secondary	Invitrogen	A-11007	Goat	N.A.	Alexa 594
Anti-Chicken Secondary	Invitrogen	A-11039	Goat	N.A.	Alexa 488

Table S9. List of primers used in this study.

Gene	**F/R**	**Sequence**
Kmt2d floxed allele (genotyping)	F	ATTGCATCAGGCAAATCAGC
	R	GCAGAAGCCTGCTATGTCCA
Kmt2d null allele (genotyping)	F	GTTCACTCAGTGGGGCTGTG
	R	GCAGAAGCCTGCTATGTCCA
Kmt2d exon 16-17 (qPCR)	F	GACCTGCTAATCCAGTGTCG
	R	CTGCTCCACCTCATCCTCTG
Actb (qPCR)	F	GCTCTTTTCCAGCCTTCCTT
	R	TGGCATAGAGGTCTTTACGGA
Atp1a2 (qPCR)	F	CTTTGGCTGCCTTTCTGTCT
	R	AGCTTCCGAACTTCATCATAGAT
Atp2b4 (qPCR)	F	CTGACCATGGAGCAGTGGAT
	R	GGAACTTCAGAGACTTGGTAGG
Cacna1h (qPCR)	F	GTGAGCCTCTCTGCCATCC
	R	TGTCCAGCAGCAGTGTGAC
Camk2a (qPCR)	F	ATCAAAGTGACAGAGCAGCT
	R	CCTCTGGTTCAAAGGCTGTC
Casq1 (qPCR)	F	GGAATCCACATTGTCGCCTT
	R	CGGGGTTCTCAGTGTTGTCT
Cox6a2 (qPCR)	F	GCCCAGAGTTCATCCCGTAT
	R	GATTGACGTGGGGATTGTGG
Eln (qPCR)	F	CTGGTGGAGTTGGCCCTG
	R	TTAGCAGCAGATTTAGCGGC

Fxyd1 (qPCR)	F	CCGACGAAGAGGAGGGAAC
	R	CTGGCTGAGTTTCCTGGAGT
Rgs5 (qPCR)	F	TCCCTGGACAAGCTTCTCC
	R	GGCAACCCAGAACTCAAGGT
Snta1 (qPCR)	F	TGTCATCGGGCTGCTGAA
	R	GTGAAGCCCTTGTCGATGTG

(IV) Supplementary references

Landt, S. G., Marinov, G. K., Kundaje, A., Kheradpour, P., Pauli, F., Batzoglou, S., Bernstein, B. E., Bickel, P., Brown, J. B., Cayting, P., et al. (2012). ChIP-seq guidelines and practices of the ENCODE and modENCODE consortia. *Genome Res* **22**, 1813–31.

Langmead, B. and Salzberg, S. L. (2012). Fast gapped-read alignment with Bowtie 2. *Nat Methods* **9**, 357–9.

Li, H., Handsaker, B., Wysoker, A., Fennell, T., Ruan, J., Homer, N., Marth, G., Abecasis, G., Durbin, R. and Subgroup, 1000 Genome Project Data Processing (2009). The Sequence Alignment/Map format and SAMtools. *Bioinformatics* **25**, 2078–2079.

McLean, C. Y., Bristor, D., Hiller, M., Clarke, S. L., Schaar, B. T., Lowe, C. B., Wenger, A. M. and Bejerano, G. (2010). GREAT improves functional interpretation of cis-regulatory regions. *Nat Biotechnol* **28**, 495–501.

Neph, S., Vierstra, J., Stergachis, A. B., Reynolds, A. P., Haugen, E., Vernot, B., Thurman, R. E., John, S., Sandstrom, R., Johnson, A. K., et al. (2012). An expansive human regulatory lexicon encoded in transcription factor footprints. *Nature* **489**, 83–90.

Ramírez, F., Dündar, F., Diehl, S., Grüning, B.A., and Manke, T. (2014). deepTools: a flexible platform for exploring deep-sequencing data. *Nucleic Acids Res* **42**, W187-89.